Laboratory Modeling of Surface Deformation Induced by the Emplacement of a Laterally Propagating Dyke

Implications for Geodesy

Daniel Abrahamsen

A thesis presented for the degree of

Master of Science

60 credits

Department of Geosciences

Faculty of Mathematics and Natural Sciences

University of Oslo

15.06.2020

Supervisor(s): Olivier Galland (PGP, UiO) and Frank Guldstrand (PGP, UiO)

Laboratory Modeling of Surface Deformation Induced by a Laterally Propagating Dyke.

Implications for Geodesy

This work is published digitally trough DUO –"Digitale Utgivelser ved UiO"

http://www.duio.uio.no

Acknowledgements

I want to dedicate this Thesis to all the fantastic people I've been fortunate to work with during the completion of this Thesis. I feel very privileged to work in such a cool and professional environment offered at Physics of Geological Processes at the University of Oslo.

My main supervisor Dr. Olivier Galland for your discussions and feedback during difficult times. Your enthusiasm and honest opinion, both of and on subject, have been of great importance to me. And for giving me freedom during my writing.

My Co-supervisor Frank Guldstrand for helping me with all technicalities related to the Thesis. Your way of thinking and enthusiasm is just remarkable and it is highly appreciated.

To "uncle" Håvard Svanes Bertelsen for the help and motivation to the laboratory aspects at the beginning of my Thesis. I sincerely hope you are doing well in life after completing your Ph.D.

To my classmates for sharing both frustrating experiences and laughs during our studies. I would like to especially thank Aleksandra Czekaj and Torjus Lømo Ellingsen, my fellow classmates, for discussions of mostly non-related topics but also your passion for the field of geology.

Finally, I would like to thank my family for endless support during my studies and respect for my academic choice. Most importantly, for putting up with my incomprehensible rambling about what I actually study. Especially you, mom. Thank you. The whole process has been one big rollercoaster, but every ride must come to an end.

Daniel Abrahamsen

University of Oslo, 15.06.2020

Abstract

An essential aspect of hazard mitigation of volcanic environments is to understand the propagation mechanisms within the volcanic plumbing system. Where dykes propagate, the eruption starts, which can have dramatic consequences for life on Earth and the environment. Dykes that breaches its way through the Earth's unexplored pathways are accompanied by deformation expressed at the surface. Understanding the linkage between subsurface processes and the associated surface deformation is thus of great importance for hazard mitigation. In this Thesis, we present an experimental model to investigate the influence of a laterally propagating dyke and the related surface deformation. Monitoring of the surface deformation is integrated through photogrammetric analysis based on four synchronized cameras, which provide high spatial and temporal resolution of the model surface. The laboratory data are compared to commonly used geodetic models to test the physical validity of such models. Geodetic models are often based on simplistic assumptions and commonly overlook the lateral propagation of dykes, despite the occurrence of such dykes within the Volcanic Plumbing System. To overcome this, we present a laboratory approach that provides insights into the related surface deformation and the emplacement mechanisms behind laterally propagating dykes, which might impose a challenge to the physical validity of widely used geodetic models.

Contents

1 Introduction

1.1 Motivation and aim

Volcanoes can pose great threats to humans. In some conditions, the volcanoes can erupt, which can have dramatic consequences for both the life on Earth and the environment (e.g., Robock, 2000). Active volcanism also plays a significant role in continental rift systems and plate divergence at mid-ocean ridges (e.g., Wright et al., 2016; Rivalta et al., 2014). Anyone that has ever witnessed a volcanic eruption is probably dazzled by the sight and complexity of such fascinating processes of nature. Arguably more complex are the processes that govern these eruptions. Processes that happen deep within the Earth, acting as a network of elaborate interactions that consequently lead to the volcanic environments expressed at the Earth's surface. Before the magma erupts at the surface and explodes into our atmosphere, it breaches through several kilometers of lithosphere, after buoyantly rising through an intricate journey into the unexplored pathways below Earth's surface. On its journey, the magma cools, crystallizes, and interacts with the host rock (Dzurisin, 2007). A series of geochemical, hydrothermal, and geophysical processes occur that consequently are coupled to the volcanic activity revealed on the surface. Through a series of complex processes later, magma can breach the surface and constitute to the dazzling yet intimidating structures of volcanoes.

Volcanoes are often recognized by the cone shape that encompasses threatening hot magma, which can sometimes protrude the surface. This surface expression is linked and controlled by processes that happen deeper within the Earth's crust (e.g., Guldstrand, 2018). An understanding of these processes and the complexity of magmatic conduits and reservoirs are increasingly growing. During the last few decades, investigations of such geological systems have been skyrocketing, imposing new techniques and tools to help scientists understand volcanoes and the processes governing them.

Monitoring experience shows that volcanoes are accompanied by measurable changes in the surface deformation produced by the subsurface processes (e.g., Dzurisin, 2007). With the use of new techniques and tools such as geodetic, seismic techniques, and laboratory experiments, scientists can get a better understanding of the complexity that lies within our Earth, which is a result of the deformation observed on the surface. The arrival of new magma and the associated

surface deformation is often a precursor to volcano eruption (Sigmundsson et al., 2018). An increasing understanding of these processes can help mitigate hazards. If future advances in the field still grow, scientists might be able to predict volcanic eruptions, which is essentially the ultimate goal of volcanology.

The relationship between surface deformation and the subsurface processes can be implemented through analytical models of source deformation (e.g., Okada, 1985; Mogi, 1958). Analytical models or geodetic models are mathematical models that calculate surface deformation from a source with known parameters such as position, shape, and kinematics. Geodetic models are often used to fit the observed surface deformation with a plausible deformation source. The best fit represents the model of which adequately reproduces the observed surface deformation.

Another approach to study the relationship between surface deformation and subsurface processes is through laboratory modeling. Laboratory experiments investigating surface deformation induced by dyke emplacements have been performed through several studies (e.g., Abdelmalak et al., 2012; Trippianera et al., 2014; Trippianera et al., 2015; Daniels & Menand, 2015: Galland et al., 2012; Bertelsen et al., 2019). Such studies have provided a dynamical investigation of alternative ways of dyke emplacement.

The laboratory data from the observed surface deformation can be compared to geodetic models and to nature to compare similarities and differences of surface deformation. Geodetic measurements simulated in the Okada (1985) forward model have characteristic surface deformation patterns that exhibit two lobes of uplift separated by a trough above the dyke (fig 2.12). Analytics of geodetic data derived from laboratory experiments are commonly used in comparison with this model. These are simplistic models that represent instantaneous inflation or deflation, but not the propagation mechanisms (Bertelsen et al., 2019). Utilizing physically relevant geodetic models requires involving intrinsic parameters such as the propagation mechanisms, which inevitably control the way dykes propagate (see e.g., Galland et al., 2018 for parameters affecting dyke propagation).

The dyke propagation mechanism is often described as propagating fractures in an elastic host rock material (e.g., Rubin, 1995; Bertelsen et al., 2019). In this mechanism, inelastic deformation is often neglected because of the small process zone concentration at the tip of the intrusion. Most models also account for vertical propagation of dykes following Linear Elastic Fracture Mechanics (LEFM).

Magma can stall and flow in various regions within the Earth's crust. The formation of new pathways and pressure changes in magma conduits, stress, and deform the host rock. Recent models show that the Coulomb properties of crustal rocks have a significant impact on the emplacement of dykes and the resulting surface deformation (Guldstrand et al., 2017). Geodetic and seismic data indicate that dykes in Hawaii and Iceland intrude laterally from shallow magma reservoirs into rift zones (Rubin, 1993). If the magma within dykes (if pressurized) becomes neutral or negative buoyancy, it can propagate laterally (Rivalta et al., 2014). It has for a long time been believed that sills were emplaced from dykes and intruded because of neutral buoyancy (Galland et al., 2018).

However, no laboratory models have been able to simulate sill emplacement propagating laterally from a dyke with neutral buoyancy (Galland et al., 2018). All laboratory models require mechanical layering of the host rock, which is often observed in volcanic environments (Galland et al., 2018). Experiments from McGuire and Pullen (1989) tested the effects of anisotropic loading on dyke propagation and showed that shallow dykes below edifices could propagate laterally to account for lateral fissure eruption. Laterally propagating dykes is also confirmed by experiments from Kervyn et al. (2009) that show a deflection away from the edifice summit. The experiment is in agreement with the lateral propagation direction observed at volcanoes and is consistent with theoretical analyses of Pinel and Jaupart (2000). The geodetic data provided by this study signifies that dikes at shallow depths can propagate laterally for up to several tens of kilometers, while erupting locally or not at all (Sigurdsson & Sparks, 1978).

Furthermore, field observations from the Bárðarbunga volcanic system support more evidence for lateral magma flow. In August 2014, a big volcanic unrest began at Bárdarbunga. Seismic activity showed that some clusters of swarms which exhibited a lateral propagating behavior associated with dike intrusions (Heimisson, 2015). These interpretations were later confirmed by GPS observations at the Bárdarbunga volcanic system (fig. 1.1). The aforementioned statements signify that magma does not always propagate upwards and can propagate laterally within the Earth's crust, which will inevitably affect the resulting surface deformation.

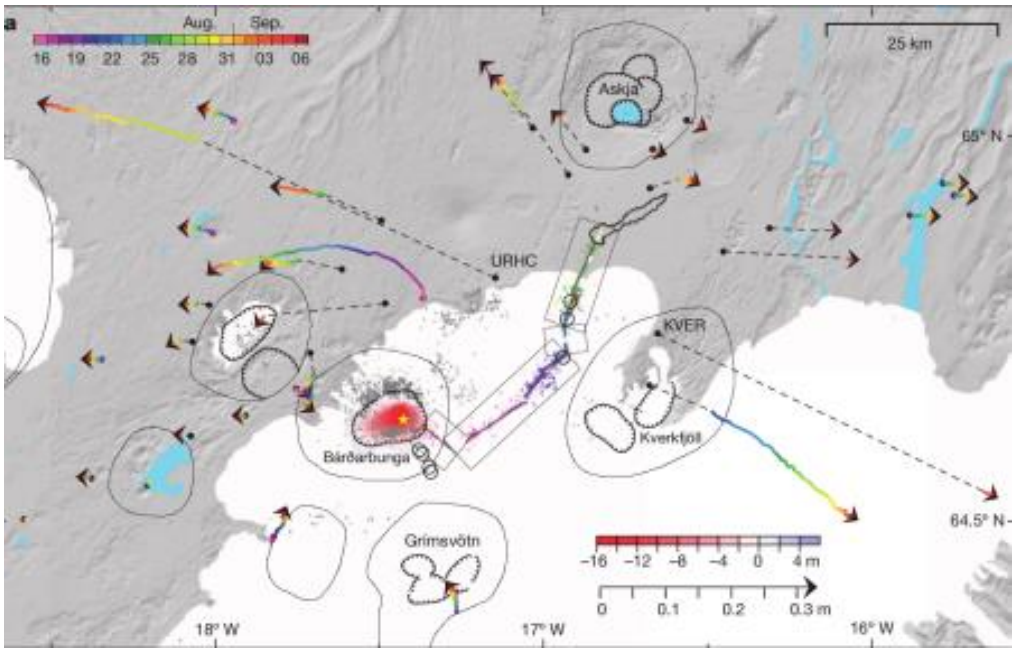

Figure 1.1: Earthquakes (dots) from 16th of august to 6th of September 2014 and GPS observations (arrows) measuring horizontal displacement located around central volcanoes (oval outlines) and calderas (hatched). Epicenters and displacement associated with the dyke are colored according to time (top left corner). The red to blue color bar (bottom right corner) shows subsidence at the Bárdarbunga caldera (reprinted from Heimisson, 2015).

There are little geodetic and seismic data that previously have been interpreted in terms of laterally propagating dykes (Heimisson, 2015). To our knowledge, there is still a knowledge gap between the influence of lateral magma propagation on surface deformation addressed by laboratory models. Because of the extensive occurrence of laterally distributed magma within the Volcanic Plumbing System, it is thus of great importance to understand the impacts of such propagation mechanisms on surface deformation. The measured surface deformation is subsequently linked to the depth of the propagating intrusion. Predicting the paths of propagating dykes and monitoring the associated surface deformation are crucial parameters to understand eruption forecasting and to evaluate hazard potential (Heimisson, 2015). This leads to the following questions, which build the aims of this Thesis: (1) To what extent does the lateral flow of magma control geodetic signals? The outcome of this project will be implemented into the context of a bigger perspective to try to answer (2) the contribution of lateral magma propagation on surface deformation and what this imposes for volcano geodetic implications? (3) What do our results impose to the physical relevance of the most established geodetic models? These questions build the fundamental aims of this project. This project will

aim to investigate these questions with a laboratory modeling approach to study the surface deformation induced by the emplacement of a laterally propagating dyke.

2 Background

2.1 Monitoring techniques for surface deformation

Geodesy is the study of Earth's geometric shape, motion, and gravity field. Geodetic studies provide quantifiable data of the motion and deformation of the plates and are a widely used tool for hazard assessment. Geodesy has been a discipline of science since the late 1600s. In the early days, it relied on trilateration and triangulation that measured angles with several reference points. After the introduction of satellites, the application potential and the accuracy of geodetic techniques rose (Bürgmann & Thatcher, 2013). Quantifying deformation is done by multiple ground-born instruments and satellites. In combination with hazardous fieldwork, space-born methods were arguably favored. The dominant approach to monitoring volcanoes is governed by monitoring surface deformation (fig. 2.1).

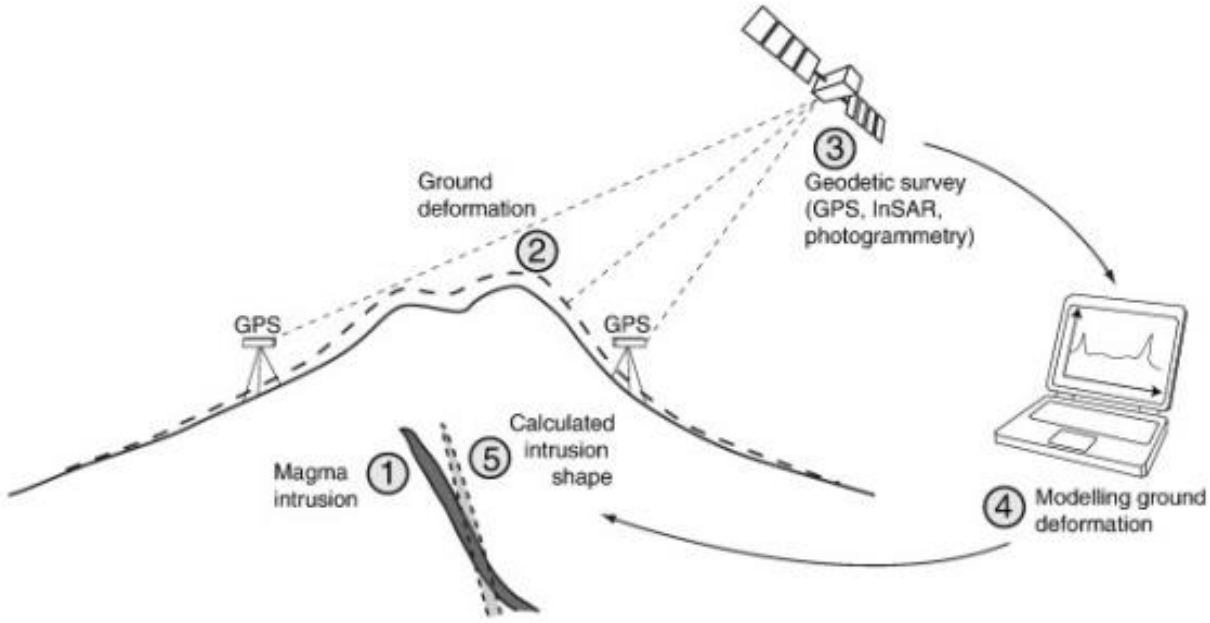

Figure 2.1: The methods that are involved during the monitoring of ground deformation and geodetic modeling in volcanic environments. (reprinted from Galland et al., 2016).

The monitoring of volcanic activity has been performed with various monitoring techniques e.g., seismicity and strain measurements in boreholes. Initially, this started with the use of triangulation and tiltmeters, which produced overall low temporal and spatial resolutions of surface deformation (e.g., Eaton, 1959). In recent times, the Global Positioning System (GPS)

and Interferometric Synthetic Aperture Radar (InSAR) were introduced, which gave rise to a higher level of accuracy and precisions in the measured surface deformation (e.g., Tong et al., 2013). Both GPS and InSAR are the most governing tools for surface monitoring today.

Volcanoes are vast structures that can range up to several hundreds of kilometers (Galland, 2012). Volcanic environments are often inaccessible because of the large extent of volcanic formations, which can induce challenges in monitoring the behavior of such structures. However, monitoring of volcanoes holds tremendous potential because the intrusions that propagate in the Earth's crust almost inevitably produce surface deformation that fingerprints the subsurface intrusion (fig. 2.2) (Dzurisin, 2007). In other words, the propagation of magma within the Earth's crust is expressed at the surface in volcanic environments. Magma that moves within the Volcanic Plumbing System triggers surface displacement, which can vary in lengths of meters to few millimeters (Galland, 2012). Monitoring and analyzing surface displacement can help provide details about the subsurface processes. Surface data are interpreted with analytical and numerical models using a plausible deformation source as the origin (Galland, 2012).

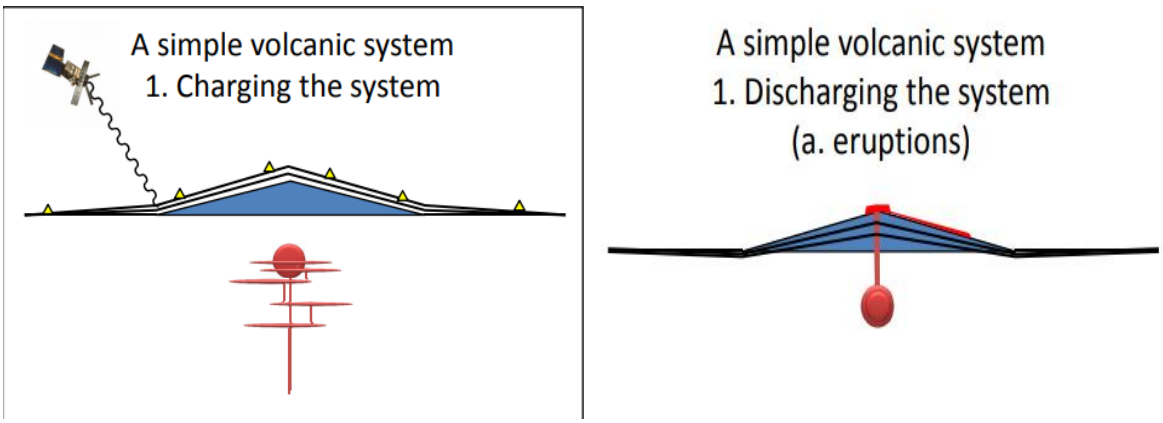

Figure 2.2: Portrays how magma build-up is charging the system, causing a bulge at the surface, which can be monitored through various monitoring techniques (left). The right figure shows how eruptions will discharge the system (reprinted from Wright, 2013). Both magma build-up and eruptions affect the geological system, which is expressed at the surface in volcanic environments.

An adequate characterization of the displacement field can accordingly give distinctive information that reflects both the geometry and location of the intrusion source. A full characterization of the surface deformation in space and time includes location, volume, and the shape of the subsurface body (Dzurisin, 2007). With detailed knowledge of the subsurface

intrusion in combination with a complete surface characterization can provide helpful insights into volcanic hazard mitigation. It is therefore of great importance to utilize adequate monitoring techniques, which provide detailed information on the surface characteristics coupled to the subsurface body. To fulfill an adequate characterization, it is necessary to provide constant and precise measurements (Dzurisin, 2007). Fortunately, monitoring and data accumulation from remote sensing systems have increased during the last decades, which has provided fundamental insights into the field of intrusive processes and the associated surface deformation. Consequently, geodetic monitoring offers bright and exciting insights to those who want to study the unstable grounds of restless volcanoes.

Figure 2.3: The infamous Mount St. Helens bulge before the eruption of 18th of May, 1980. Scientists measure bulges at volcanic flanks produced by the subsurface magma that consequently deform the surface. The monitoring of volcano deformation is valuable for volcanic hazard mitigation (Photo credit: Peter Lipman, USGS).

2.1.1 Tiltmeter

One of the oldest methods of measuring surface deformation of volcanoes is by the use of tiltmeters. A tiltmeter is placed on the Earth's surface and measures changes in the inclination of the surface. The tiltmeters contain conducting fluids, bubbles, and sensors. The bubbles measure changes in conductivity that are created from small tilting movements in the tiltmeter. Conductivity changes are directly linked to the magnitude of tilt (Dzurisin, 2007).

Long-base tiltmeters are used over larger extents and generally have higher precision, which can measure gentle changes in tilt over several years. The encased fluid surface remains horizontal as the tiltmeter is tilted. The change in tilt creates an offset that measures movements in volcanic environments (fig. 2.4) (Dzurisin, 2007). It is generally a less expensive method and yields continuous, real-time data output in which the processing power for obtaining the tilt data is not substantial compared to the following monitoring techniques.

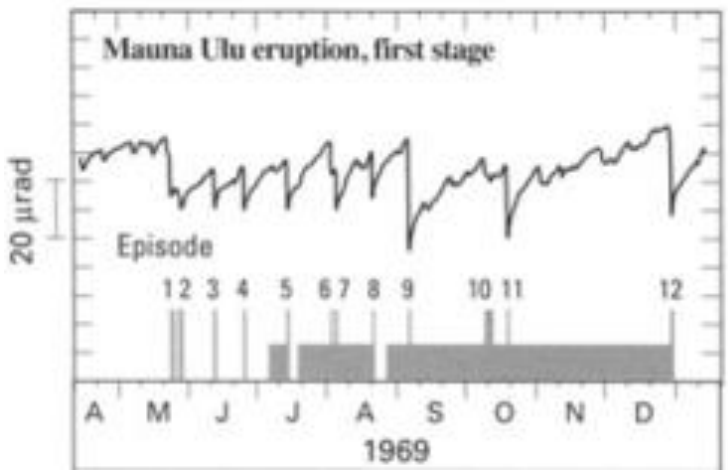

Figure 2.4: Shows west-east tiltmeter records placed on the summit of the Kilauea volcano in 1969. Full height bars represent episodes of eruption characterized by high volume magma discharge and half-height bars represent low volume effusive activity (Reprinted from Dzurisin, 2007).

2.1.2 Aerial Photogrammetry

Aerial photogrammetry is a technique used to calculate the shape, size, and position of an object from a cross-domain fusion of measurements from 2D images. By combining information about the 2D images, 3D coordinates of points of interest can be constructed from optical triangulation of two or more images at different angles relative to each other. If performed correctly, this method can create high-resolution images of surface reconstructions by combining different topographic images. Geoscientists have, for a long time utilized 3D data from photogrammetric techniques. Such data has been used to visualize the Earth's surface and extract surface data from aerial photographs (e.g., Birdseye, 1940). Photogrammetric techniques were significantly improved when fundamental principles of photogrammetry and robust computer algorithms started. Collecting overlapped images can be easily extracted and

automatically processed, constructing 3D-models from millions of surface points (Bemis et al. 2014). Photogrammetric surveying relies on capturing images at a constant altitude that requires a minimum 60% overlap between each image (fig. 2.5). Several flight passes are done to ensure full image coverage of the area. Each passing has a side lap of about 20-30%. Aerial photography is classified as nadir or oblique, depending on the camera direction relative to the ground. A combination of these two gives the best aerial images (Thompson & Schilling, 2007).

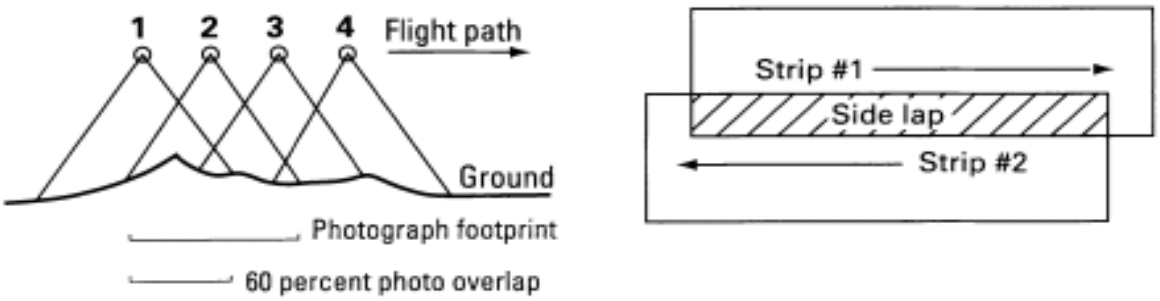

Figure 2.5: Geometric representation of photogrammetry. The images have a 60 percent overlap (left) and 20-30 percent overlap for the adjacent photo strips (right) (reprinted from Dzurisin, 2007).

Aerial photogrammetry is a powerful tool that is used to generate digital elevation models (DEM) and orthophotos in high-resolution (limitations of photogrammetry are described in section 6.4). DEMs give an insight into estimations of mass movement and physical surface changes (fig 2.6) (Fabris & Pesci, 2005). An orthophoto is derived from several aerial images and is photogrammetrically rectified.

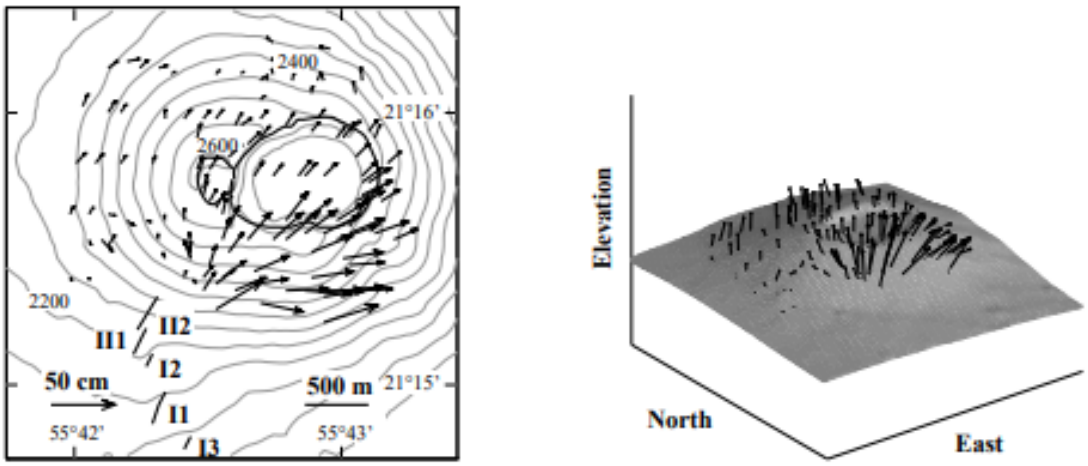

Figure 2.6: Ground displacement modeled by photogrammetric survey at Piton de la Fournaise Volcano, Reunion Island in 1981. The left figure shows a map view of contours at

50 m elevation. The right figure shows an oblique perspective. I1, I2, I3 are eruptive fissures after rupture episodes. (Reprinted from Cayol et al., 1998).

2.1.3 Interferometric Synthetic Aperture Radar (InSAR)

Interferograms created using SAR satellites can cover large areas and measure precise surface deformation without going to the field (Bürgmann & Thatcher, 2013). Synthetic Aperture Radars implements signal-focusing techniques with satellite information resulting in high-resolution radar images (Bürgmann & Thatcher, 2013). InSAR calculates the distance in line-of-sight (LOS), and the topography on the surface for multiple satellite passes. Each passage covers about 100 km in width. SAR creates radar images giving information on the amplitude and signal phase in the pixels. The phase offset between two satellite scans is measured by the change in wavelengths from the radar. The change allows the creation of interferograms for SAR images that calculate the surface displacement of time intervals between images (fig. 2.7)(Dzurisin & Lu, 2007). InSAR provides a map of difference in phases.

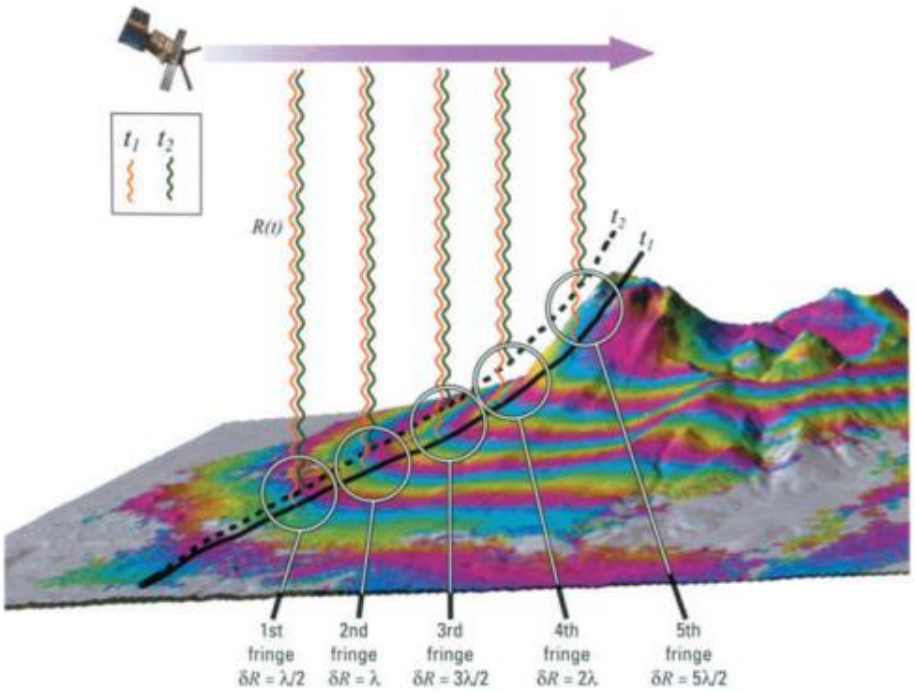

Figure 2.7: The figure shows an inflating volcano that produces concentric fringe pattern in a radar interferogram. The distance between the satellite and the ground changes as the satellite passes such that the change in distance of half a wavelength represents one fringe. Surfaces that exhibit subsidence will show the same pattern, but the fringe pattern is inverted. (Reprinted from Dzurisin & Lu, 2007).

This technique is suspectable to a large number of errors that challenge the precision, accuracy, data acquisition and deformation maps. Parameters affecting errors include e.g., vegetation, erosion, baseline length changes that cause decorrelation between image passes, thus leading to a loss of information (Bürgmann & Thatcher, 2013). Satellites also operate at different wavelengths that delay travel time as it passes through the atmosphere, which can disturb the output data.

2.1.4 Lidar

Lidar, or light detection and ranging, is a remote sensing technique that uses the combination of lights and radars used to measure the position of an object (Dubayah & Drake, 2000). This technique calculates the time difference between an emitted laser signal and the reflected light. The instrument uses lasers on a target area and measures the round-trip time for the laser pulse to a target and back to the sensor. Analyzing the travel time of the pulse from the time of initiation until it is reflected back to the sensor, the distance from the measured object can be calculated (Ralph et al., 2000). Lidar scanners are generally used for long distances and precision. It produces high-resolution maps with horizontal and vertical data with high vertical accuracies (Lim et al. 2003). Lidar data are used to analyze ground structures to make detailed 3D models, which provides valuable data to interpret the ground motion of an area of interest.

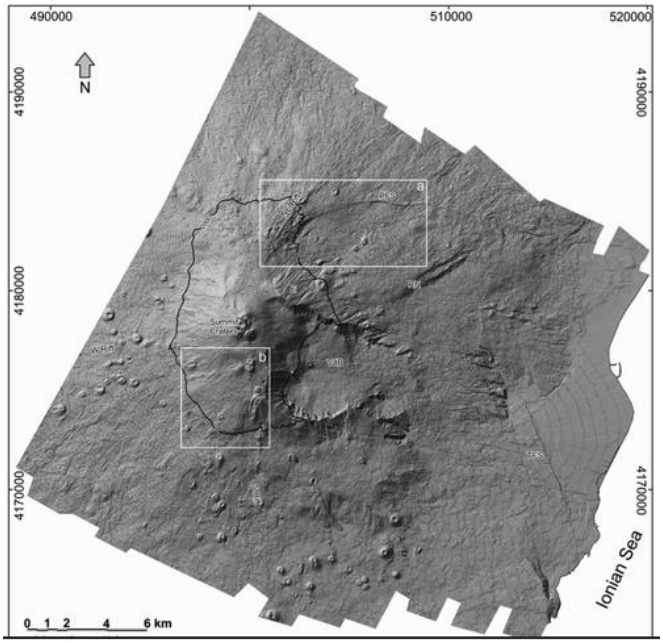

Figure 2.8: A digital terrain model of the Mt. Etna volcano produced by Lidar modeling showcasing the morpho-structural features of the Mt. Etna volcano. The grey lines are contours of 25 m (reprinted from Bisson et al., 2015).

Errors often arise from Lidar scanning with steep uneven terrains and the costs can often be expensive. It is also time-consuming and it is a campaign style monitoring technique. However, this technique can provide sub-decimeter accuracy point data (Dzurisin, 2007).

2.1.5 Global positioning system (GPS)

GPS is an excellent tool for providing data about velocities and positions. It was first used for the military, but people quickly recognized its potential for scientific use. The GPS consists of 24 satellites orbiting the earth (figure 2.9). The network of 24 satellites makes it possible to gather enough information to determine the position at any place and time on the Earth's surface. The principle of GPS is to measure the time from a satellite signal from about 20 000 km height to a receiver on the ground. Since the velocity of the signal is the speed of light, one can convert the travel time into distance (Bürgman & Tatcher, 2013).

Figure 2.9: A network of GPS satellites consisting of 24 operational satellites in six orbit planes (reprinted from Dzurisin, 2007).

Each satellite sends two signals with a wavelength of 19 and 24 cm. To determine the position of the receiver on the ground, one needs to know the position of each satellite. A network of reference stations measures the orbits of the satellites. Each receiver can detect four or more satellites. With information about time and position from each satellite, a three-dimensional position is calculated (Bürgman & Tatcher, 2013).

GPS is frequently used for measuring surface deformation in volcanic environments. Figure 2.10 below shows the volcano inflates (left) and rises (right) as the magma chamber pressurizes. Points A, B, C, and D are GPS stations that move, during inflation, to points A', B', C', and D'. This movement can be tracked and used for hazard mitigation. GPS stations provide vector data of surface displacement. Tiltmeters installed at the flanks of volcanoes, measure the change in tilt as a result of a pressurized magma chamber.

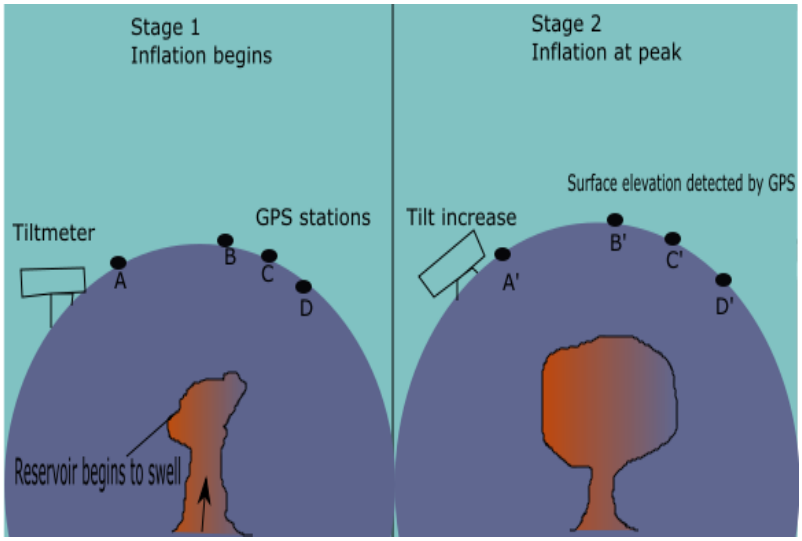

Figure 2.10: GPS and tiltmeters as the magma reservoir inflates. GPS measures the motion as the magma chamber inflates or deflates. GPS diagrams are shown in the right figure where the vectors describe horizontal motion, and the colors show vertical motion (recreated from Jessica Murray-Moradela from USGS).

GPS provides long term 3D vector space displacements and greater temporal resolution compared to InSAR, which offers global coverages and high spatial resolution (Bürgmann & Thatcher, 2013). For an extensive review, see e.g., Dzurisin (2007). GPS measurements from field monitoring at the Kilauea volcano eruption are shown in figure 2.11.

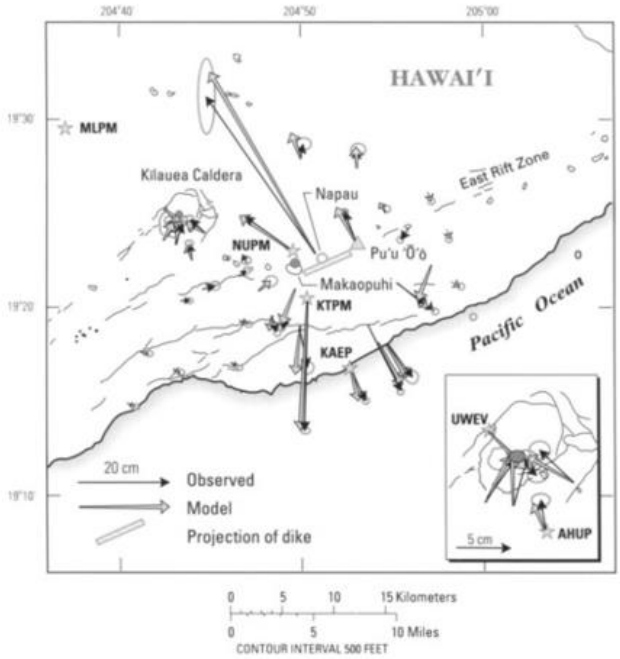

Figure 2.11: Horizontal displacement maps produced by continuous GPS stations at the Kilauea volcano eruption in 1997. Black arrows represent GPS displacement and grey arrows represent model prediction displacements. Stars with four letters designate GPS stations. Thin lines represent faults, fractures and fissures (reprinted from Dzurisin, 2007).

2.2 Analytical source models applied to surface deformation

The surface deformation measured by geodetic models can be modeled in mathematical models called geodetic models. Such models have over the years advanced with improved computing powers and optimizations in volcano monitoring techniques. Geodetic models are simplistic mechanical models based on a set of physical assumptions. The models commonly assume the processes are described as an emplacement of a magma body with uniform properties and idealized geometries, surrounded by a homogenous, isotropic host rock in an elastic half-space (Sigmundsson et al., 2018). Most models also assume linear elastic deformation of the host rock rheology, neglect thermal processes and magma rheology changes (Rivalta et al., 2014). These models lay the foundation of an approximated Earth with forces and dislocations as sources of deformation (Lisowski, 2007). These sources can be tectonic and volumetric. The volumetric sources are deflating or inflating bodies, and tectonic are strike-slip and dip-slip fault dislocations. A combination of these can achieve a suitable model.

Fitting real world and geodetic surface displacement, one can achieve approximations of the parameters including geometry, location, and dynamics of the subsurface source, which are all essential parameters to understand for hazard mitigation. However, producing such solutions provide non-unique solutions, i.e., several sources can reproduce the observed data creating uncertainties in the interpretations.

An important aspect when creating geodetic models is the approximation of the crust, which includes recreating a medium in which the processes acts. The most common way to simulate the crust is through an elastic half-space, which is semi-infinite in the vertical dimension and infinite in the other. It is also isotropic and homogeneous such that Hooke's law can be applied, i.e., a linear relationship between stress and strain. Tests suggest that rock at low temperature are approximated as linear elastic for strain below 1% (Lisowski, 2007). With such an approximation, many sources of geodetic models are made. For the purpose of this Thesis, we will consider two commonly used geodetic models described below (table 2.1 & fig. 2.11). A comprehensive description of other widely used geodetic models is done by, e.g., Dzurisin 2007; Sigmundsson et al., 2018.

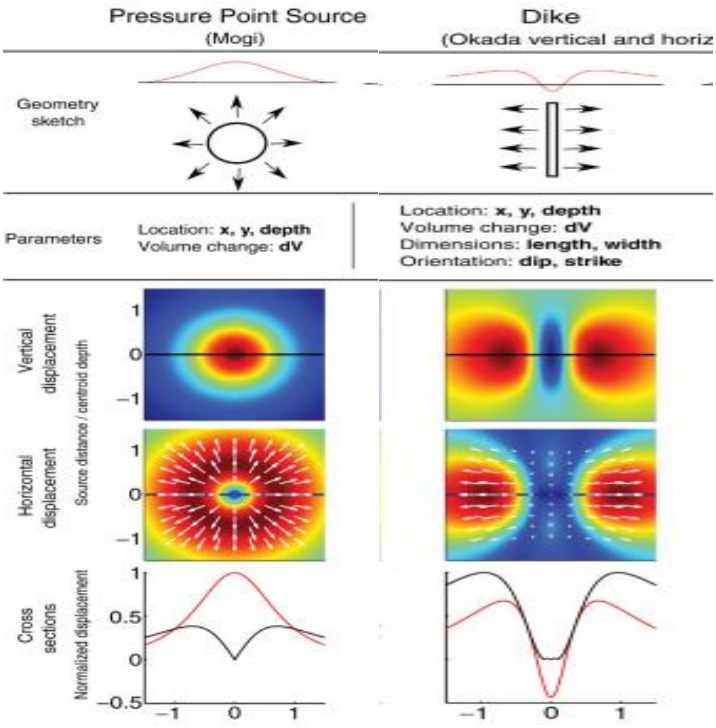

Figure 2.12: Illustration of the analytical models of Mogi (left column) and Okada (right column) and the predicted surface deformation pattern produced by the analytical models. The horizontal (black) lines and vertical (red) lines are normalized with maximum displacement and the source distance/centroid depth (reprinted from Sigmundsson et al. 2018).

Table 2.1: Main analytical models for magma sources within an elastic half-space and the main assumptions. The table provides differences between the two models from Mogi (1958) & Okada (1985).

Geodetic model	**Okada (1985)**	**Mogi (1958)**
Output	Surface deformation due to a planar rectangular dislocation	Surface deformation due to a pressurized spherical cavity
Main Assumptions	Uniform opening (for dykes/sills) on a rectangular dislocation. Isotropic elastic half-space	Isotropic elastic half-space where the depth of the point source is much greater the radius of the point source. Incompressible magma.
Differences	Sphere radius a<< sphere depth (d). Pressure applied to cavity walls: Stress boundary conditions in the cavity	For dykes, tensile displacement only Displacement applied to dislocation: kinematic boundary condition in dislocation
Model results	Uplift only	Elongated subsiding through above dislocation surrounded by two uplifting bulges of planar symmetry

2.2.1 The Mogi point pressure source

The geodetic model describing the inflation or deflation of a magma chamber is commonly referred to as the Mogi source. Surface displacement of eruptive events measured at sites in Hawaii and Japan, can be linked to dilatational or compressional forces in an isotropic elastic half-space. Mogi (1958) proposed a mathematical solution for the surface displacement based on a cavity which is hydrostatically pressurized by incompressible magma. This source model gives the relationship of the deep magma spherical body and the doming at the surface, assuming a small sphere size relative to the burial depth of the sphere (figure 2.13).

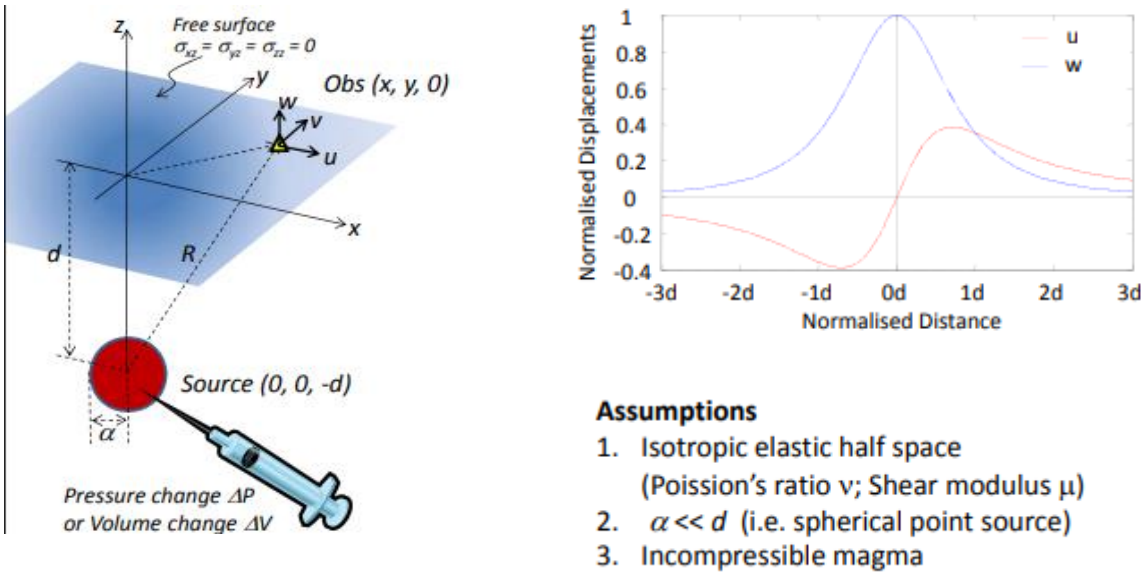

Figure 2.13: The Mogi model with the schematic coordinates and the geometrical relationships that describe this model. The upper right corner shows the axisymmetric surface displacement from the Mogi source, where the red line shows horizontal displacement and the blue line shows vertical displacement (reprinted from Wright, 2013).

2.2.2 The Okada source

A dyke has a tabular shape where the lateral extent is much bigger than its thickness. An often used model for dykes is the Okada source model. This model represents the dislocation of a rectangle in a tensile mode or a fault with a sense of shear often commonly used for earthquake-related deformation.

Davis (1983) showed that deformation produced by a tensile dislocation with the shape of a rectangle and a certain dip could approximate a crack in nature. Later derivations by Okada is now more commonly used.

Dyke intrusions are approximated in two ways in a tensile mode. The first is by a point, and the second is by a rectangle. Deformation caused by a rectangular crack in which the depth is smaller than its width is approximated by the point model. This model shows variations in displacement with a varying dip of the crack. At dips close to 0 degrees, a symmetrical pattern develops at the surface. Increasing dip gives increasing deformation asymmetry.

Most geodetic models are simplistic models that suffer from a lot of limitations. More realistic Earth models have been developed to account for curvature, topography, gravity, vertical layering and lateral inhomogeneity. It is believed that continued advancement in the field and improvements in geodetic data quality will lead to more widespread use of such realistic models. The physical relevance of the main geodetic models will be discussed in section 6.2.

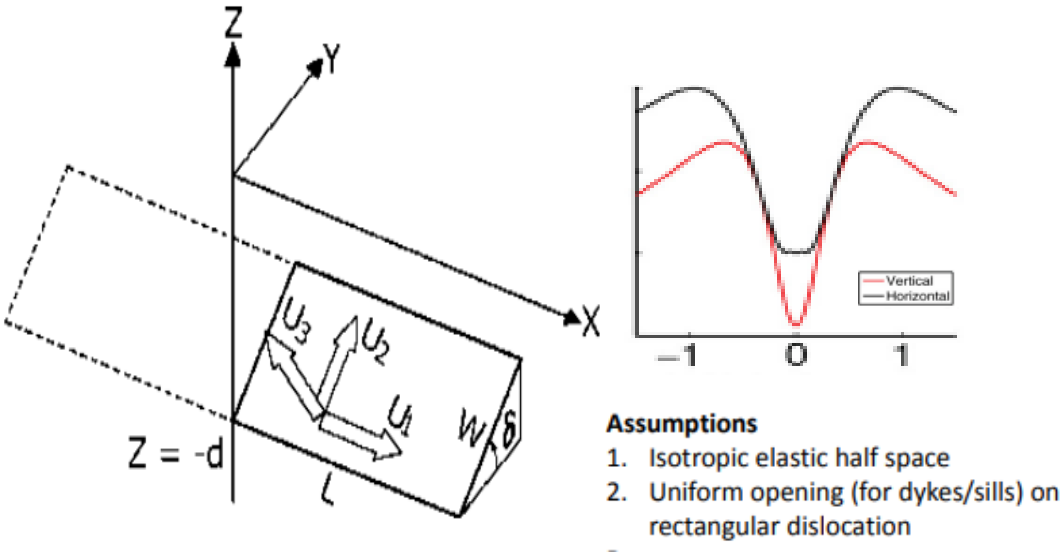

Figure 2.14: The Okada model with the corresponding coordinate system used in the Okada Source model (left). The figure shows a rectangular tensile dislocation at depth d with a half-length L. The sheet strike along the x-axis and a dip angle δ from the horizontal. The tensile dislocation defines a down-dip width W, length L, and uniform opening U_3. The upper left figure shows surface displacement where the red corresponds to horizontal displacement, and the blue corresponds to vertical displacement (reprinted from Dzusirin, 2007; Wright, 2013; Heimisson, 2015).

2.3 Dyke propagation mechanisms

Previously, this chapter has described the volcanoes and the study of volcano monitoring of the surface on a broad scale. On the other side, it is also of great importance to understand volcanic processes in the subsurface because these processes are directly linked to one another. To help understand the complexity and processes of volcanoes, it is also essential to delve down into the Earth and understand what happens within the Earth's crust. Magma inside the Earth is composed of a network of conduits and reservoirs, often referred to as the Volcanic Plumbing System (VPS) (Fig. 2.15). This system transports and stores magma within brittle or ductile Earth materials, characteristic of Earth's upper lithosphere (Galland et al., 2018). The volcanic plumbing system is a complex system generated by chemical, thermal and mechanical

processes between the magma and the crust that hosts it. These processes within the VPS can happen from milliseconds to millions of years, and at length scales of microns to several thousands of kilometers (Galland et al., 2018).

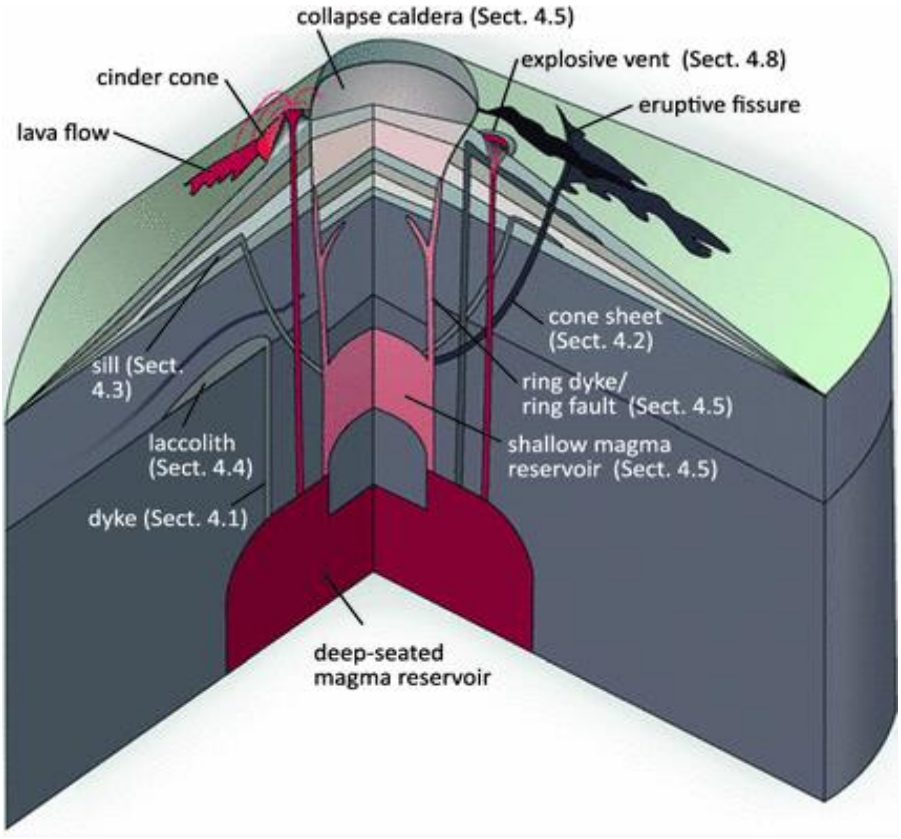

Figure 2.15: Illustration of the main characteristics of the Volcanic Plumbing System. (Reprinted from Galland et al., 2018).

A significant part of the VPS are dykes that facilitate the vertical (or lateral) ascent of magma. The magma transport that happens in the brittle crust occurs by dyking (Rivalta et al., 2014). Dykes are planar sheets with an aspect ratio from 10^-2 to 10^-4 (Rubin, 1995). Such structures can be found in a range of tectonic settings and encompass a wide range of compositions. Dikes are commonly sub-vertical sheets that have predominantly tensile mode (Mode I) fracture with little shearing (figure 2.16). They are often found in swarms and can extend for tens to hundreds of kilometers (Rubin, 1995).

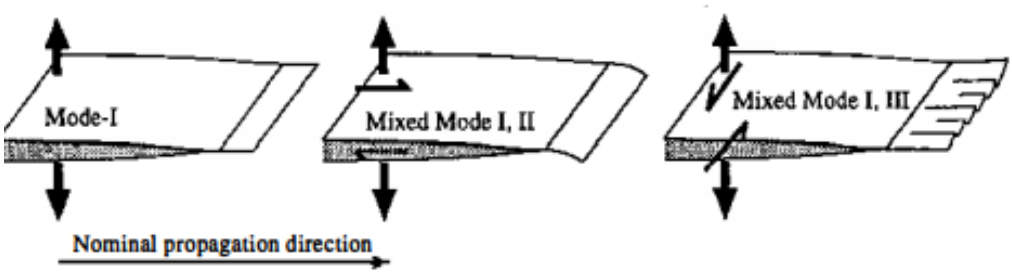

Figure 2.16: Modes of crack propagation paths under mixed-mode loading (reprinted from Rubin, 1995).

Mechanisms of magma propagation at depth influence how magma flows and communicates with the surrounding host rock. Processes of magma transport are envisioned as porous flow in partially molten and deformable source rock. Magma transport in fractures or dikes is a favorable way for magma to propagate through the cold lithosphere (Rubin, 1995). The propagation direction is favored by the least compressive stress orientation σ_3. However, dyke propagation is governed by a wide range of other factors, including driving pressure, elastic or density discontinuities, which may favor different propagation directions. Measurements of deviatoric stress are challenging, thus confirming if the dyke direction is perpendicular to σ_3 is complicated (Heimisson, 2015). When analyzing rock fracture, it is often useful to distinguish three different regions of tensile crack propagation. (1) The crack, (2) elastic deformation, and (3) the process zone of inelastic deformation (Rubin, 1995). Griffith postulated that crack propagation happens if the accompanying release of potential energy is sufficient to provide enough energy for fractures to happen. For dikes, the potential energy is the elastic strain energy and the work done to the surrounding host rock from the magma or gravity (Rubin, 1995)

In order to understand the emplacement mechanisms, insights in new magma influx, the differentiation of magma, crystallization, and assimilation of the host rock are needed (Guldstrand, 2018). Deformation is also influenced by heat exchange with the host rock, interaction with pre-existing cracks, stresses, pore pressure, and mechanical properties of the host rock such as cohesion (e.g., Rivalta et al., 2014; Guldstrand, 2018).

When magma is introduced into the system, the surrounding host rock needs to accommodate volume for the magma to be emplaced. The amount of host rock deformation will vary in nature based on how competent the host rock is. A crystalline bedrock is highly competent compared to weaker rocks, such as sedimentary rocks. This host rock characteristic will influence

deformation in the host rock, which again controls the emplacement dynamics and magma propagation (Guldstrand, 2018).

The dyke propagation mechanism is often described as propagating as elastic fractures in an elastic host rock material (e.g., Rubin, 1995; Bertelsen et al., 2019). In this mechanism, inelastic deformation is often neglected because of the small process zone concentration at the tip of the intrusion. Most models of propagating dykes also account for vertical propagation of dykes following Linear Elastic Fracture Mechanics (LEFM) despite the clear occurrence of laterally propagating dykes (described in section 1.1). Bertelsen et al. (2019) described dyke propagation in silica flour experiments that are accommodated by shear failure with inelastic compaction of the host rock. This mechanism describes dyke propagation is governed by the Coulomb properties of the host material, which is known as the viscous indenter model (fig.217) (see discussion section 6.1). This might call for the new developments in models that account for the different dyke emplacement mechanisms of laterally propagating dykes.

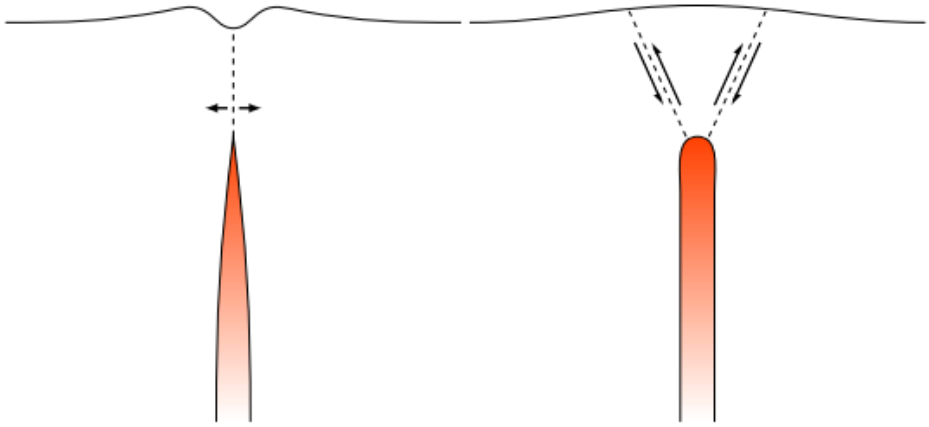

Figure 2.17: The figure shows dyke propagation mechanisms of tensile elastic (left) versus viscous indenter (right) and the associated surface deformation (reprinted from Bertelsen et al., 2019).

The VPS is a complex geological system governed by many processes. A thorough understanding of this system also emphasizes the importance of including both deformations at small-scale, i.e., at the intrusion tip, and large-scale, corresponding to the surface deformation. However, human observations are often limited. Studying processes deep within the earth requires methods that are beyond fieldwork observations. Fieldwork is commonly used by Earth scientists to understand the geological systems based on field observations and interpretations. Observations from the field is a result of many past or on-going processes (Galland et al., 2018). What is observed in the field is a combination of many processes resulting in the present field

observations. Understanding the roles of individual processes on the system's evolution might accordingly be difficult to grasp. A method to tackle these difficulties is to investigate individual processes of a system's evolution through laboratory modeling.

2.4 Laboratory modeling and model materials

Laboratory modeling can be executed in a controlled manner by varying an individual set of parameters to help understand the relative contributions of individual physical parameters on the geological system. Hence, performing laboratory experiments can be a unique and fun (or very, very frustrating) way to get a new perspective and understanding of a geological system and the processes governing the system.

Hall (1815) was arguably the first to perform analogue modeling experiments. He conducted experiments to qualitatively explain folded rock stratigraphy that was observed in Scotland. Since then, analogue modeling has been a widely used tool for Earth scientists to help understand the individual physical processes that control the behavior of the geological system as a whole.

With the aid of robust monitoring techniques, one can provide quantifiable of surface deformation derived from laboratory approaches (see Chapter 3). The implementation of surface monitoring from laboratory experiments can help validate the results obtained from such experiments. Techniques such as photogrammetry, laser scanning, and structured light have been performed during laboratory experiments. If these techniques properly utilized and the experimental conditions are properly scaled (see section 3.6), laboratory experiments have the advantage of reflecting a representative geological system in which the geometry and the surface deformation are known (Galland et al., 2018).

In order to create a successful laboratory experiment, it is important to choose relevant model materials and parameters. It is also essential to understand the mechanical properties of the materials used. This is important when creating the laboratory apparatus, setting the initial boundary conditions, and interpreting the results (Galland et al., 2018). To create an experiment that is quantitatively significant, it is also vital to consider similarities to your experiment and the natural environment so that it fits with real-world proportions. A more detailed explanation of experimental fitting with real-world dimensions will be explained in section 3.6.

Rocks exhibit a large variety of mechanical behaviors. These behaviors can yield different end-member rheologies such as elastic, viscous, plastic, and often a combination of these behaviors (Galland et al., 2018). Elastic deformation is reversible. If the stress applied to a material is released, the strain, i.e., the change in the shape of the material will return to its original shape. Elastic deformation occurs at low stresses and strains. However, rocks have certain strength limit or yield stress. If the stresses become high and overcome the rock's yield stress, the deformation of the material becomes irreversible. When the stress is released, the strain of the material does not return to its original shape. This behavior is referred to as viscous behavior. In this regime, the strain rate is a linear or power law of the applied stress (Handin, 1987). In the plastic regime, the material starts to deform once the stress reaches the yield stress. After this value is reached, the material deforms continuously and irreversibly (Handin, 1987).

A combination of these end members is exhibited in nature, making the rock behavior extremely complex and challenging to understand. Fortunately, end-member rock behaviors are dominating under certain pressure and temperature conditions over given length and time scales (Galland et al., 2018). rocks in nature are often dominated by one of the end-member rheologies. This makes it possible to simulate these mechanical end-member behaviors in the laboratory. Simulating such mechanical behaviors with laboratory experiments can provide an understanding of the rheological behavior in nature.

A common material used by Earth scientists to simulate model rocks in laboratory experiments is dry and loose quartz sand. It is plasticity-dominated and has negligible cohesion. Consequently, the material fails along shear zones, simulating faults. Failure of quartz sand occurs to the Mohr-Coulomb criterion defined by an angle of internal friction. For simulating low cohesion host materials in nature, quartz sand is the most applicable analogue for Earth's crust (Galland et al., 2018).

Another commonly used end member is elastically dominated gelatine. This material fails through the formation of open cracks. It behaves elastically, indicating irreversible deformation, except in small regions around the tips. Gelatine becomes birefringent when it is strained in crossed polarizers, which is a valuable optical property for studying stresses in the material. This material is mostly applicable for well consolidated high cohesion sedimentary rocks and small-scale processes (Galland et al., 2018).

In nature, rocks often behave at intermediate stages. Since dry sand and gelatine are end members of mechanical behaviors, both plastic- and elastic-dominated, respectively. Gelatine experiments model host rock as an elastic solid where dykes propagate as Linear Elastic Fracture Mechanics (LEFM). However, field observations show that rock behavior as a result of dyke emplacement is substantially inelastic (Galland et al., 2018, and references therein). To account for the inelastic response, other materials need to be used in order to delineate the natural system better. Finding a material that can contain such mechanical behavior are cohesive granular materials such as fine-grained silica flour (e.g., Galland et al. 2006, 2009). This material typically contains mode I and shear Mode II fractures and reproduces elasto-plastic behavior of natural rocks. It fails according to Mohr-Coulomb and is defined by tensile strength, cohesion, and an internal angle of friction (Galland et al., 2018). Most studies use end-member rock materials, but more recently, cohesive materials allowed investigating the effect of combined mechanical behaviors on magma transport (model material properties are described in Chapter 3).

2.5 Background summary and motivation for further study

This chapter gave a brief overview of monitoring techniques of surface deformation and analytical models linked to magmatic processes and the associated surface deformation. The monitoring of surface deformation at restless volcanoes is essential to unravel subsurface processes and hazard potentials because it reflects the shape and dynamics of the subsurface (Galland et al., 2018). GPS, Lidar, InSAR, and photogrammetry are complementary approaches that can provide robust geospatial products to understand surface deformation at active volcanoes. GPS produces 3D vector displacement field with temporal and spatial coverage, Lidar provides highly accurate point-level data, InSAR contributes to geometric fidelity, and photogrammetry gives realistic terrain visualization.

Geodetic data is often fitted with displacement data predicted by analytical or numerical models. Modeling of surface data can also be simulated in simplified mathematical models or through scaled laboratory models. However, these models suffer from several limitations because of the physical oversimplification to be computable efficient and because of Earth's natural complexity. The underlying causes of surface deformation at volcanoes can be addressed and interpreted by laboratory models. Most models account for LEFM and the

vertical propagation of dykes despite observations of laterally propagating dykes and inelastic deformation. This might call for the development of new models that account for these mechanisms. Consequently, this leads to our laboratory approach to gain insights into laterally propagating dykes and the associated surface deformation and its geodetic implications.

3 Methodology: Experimental modeling

3.1 Laboratory experiments

To understand the contribution of the experimental parameters on our geological system, we performed laboratory experiments. An experimental setup (fig. 3.2) was designed in order to study the effect of lateral magma propagation on surface deformation. Dyke emplacement analogues are achieved through two end-member processes: (1) Injection of vegetable oil into a host rock material and (2) forward pushing metal plates into a host rock material (e.g., Trippanera, 2014; Trippanera, 2015). In this Thesis, the focus will revolve around the injection of vegetable oil into a host rock material. Several experiments were run to test our models. Different parameters were varied in a controlled manner for the various experiments performed (see Chapter 4 for details). These experiments investigated the relative contribution of individual physical parameters on our geological system, i.e., the impact of lateral magma propagation on surface deformation.

3.2 Model materials

Silica flour (product name M400) is used as a host rock analogue in our experiments and comprises of fine-grained crystalline silica. The mechanical properties of the silica flour were measured by Galland et al. (2009). In this article, the Mohr-Coulomb failure criterion was estimated after compaction. The value for cohesion was measured to 369±44 Pa, a friction coefficient of 0.81±0.06, and an angle of internal friction of 39°.

To connect the contribution of the model magma and host rock material, we need to prevent the percolation of the model magma. It is essential to use a material that is not wettable by the fluid in question. The fluid should be chemically and physically incompatible with the host rock material it is injected into (Galland, 2006). The material also needs to follow a linear Mohr-Coulomb failure envelope, which is essentially the case for the silica flour.

Végétaline oil is used as a magma analogue (figure 3.1). It is produced by Unilever in France. The oil has a low viscosity ($\eta=2x10^{-2}$ Pa s at 50°C), simulating low viscosity magmas (Galland et al., 2006). This oil is heated to around 50°C and will solidify at room temperature, making it

possible to excavate and study the shape of the intrusion geometry. Model materials compared to nature are provided in the table 3.1.

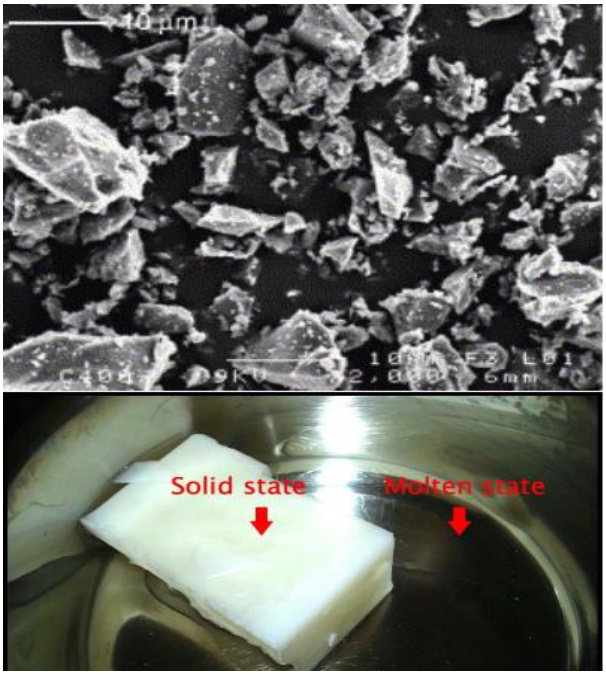

Figure 3.1: The upper picture shows the silica flour in a microscope, and the lower shows the vegetaline oil in its solid and liquid state (from Galland et al., 2006).

Table 3.1: Experimental and field parameters and their dimension (from Galland, 2012).

	Parameter definition	Field	Experiment	Dimension
C	Cohesion of brittle material	10^7->10^8	350	Pa
D	Thickness of overburden	1000->5000	0.04->0.05	m
G	Acceleration due to gravity	9.81	9.81	ms^{-2}
H	Thickness of intrusion	1-100	$2x10^{\wedge-3}$->$3x10^{-3}$	m
Φ	Angle of internal friction	25->45	39	-
η	Magma viscosity	10^2->10^8	$2x10^{-2}$	Pa s
ρ_m	Magma density	2500->2900	≈900	kg m^{-3}
ρ_r	Host rock density	2000->2500	1050	kg m^{-3}

3.3 The experimental setup

The experimental setup (fig. 3.2) consisted of a plexiglass box (40 cm x 40 cm) hosted by a central vertical inlet. The experimental setup in this Thesis was first introduced and developed by Galland et al. (2006). The inlet has a height of 3,4 cm and a circular opening (1 cm), which gives rise to the injection of magma via a volumetric pump that injects vegetable oil into the system. The velocity of the oil injection can be monitored and set to a given velocity. A constant velocity of 0.30 mL/min was used throughout our experiments. The vegetaline oil described in section 3.2 is injected into the box via the volumetric pump. The oil is heated to around 50°C before the experiment and will later solidify at room temperature to allow for excavation of the intrusion. The box is filled with 16 kg silica flour and leveled up to a given height. In order to control magma propagation, a firm net was used with a mesh size (0,5cm x 0,5cm). The net simulates a weak layer in the silica flour as it reduces the contacts between the grains in the flour. The meshed net was used to produce layering contrasts, a hypothesis that was built on fundamental gelatine experiments by Pollard and Johnson (1973), which simulated the formation of sills from vertical propagating dykes from rigidity and strength contrasts in the layered gelatine. This net was stretched horizontally and extended from one side of the box wall, over the inlet, to the other side of the box wall (see Appendix A for a complete experimental procedure).

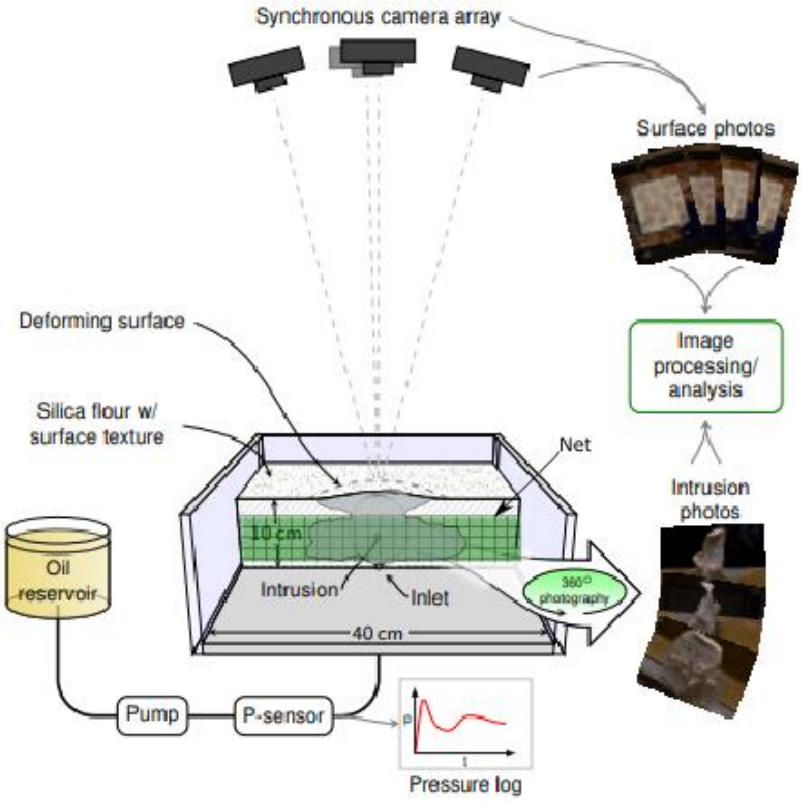

Figure 3.2: Schematic representation of the experimental setup and procedure for injecting oil into a Mohr-Coulomb material. The material used is silica flour that lies within a 40x40cm box with viscous oil injected at the inlet. The injection speed is held constant for 30 mL/min, which is controlled by a pump. The net is placed horizontally across the experimental box. The Pressure is measured with the pressure sensor. The surface deformation of the textured silica flour is monitored by four synchronized cameras directly above the model surface (modified from Bertelsen et al., 2019).

The pressure is monitored for each experiment through a pressure gauge. Water is filled in a small column that is attached to the pressure gauge, measuring the pressure at short time intervals. The experiments last until the oil reaches the surface. After the experiment, the oil is cooled and solidified. The silica flour is later carefully removed, and the solidified intrusion geometry was studied.

Preparation of the silica flour involves compacting the material to a given density. The material is put inside our glass box that is connected to a Houston vibrator (model GT-25). A metal plate is placed on top of the material to produce an initially flat surface. It is compacted to have a density of around 1050 kg/cm^3. Silica flour density is calculated by measuring the silica flour depth from the top of the box for each corner. As the mass of the silica flour that is poured into the box is known (16 kg), density can be calculated. After compaction, the material is more cohesive and sustains vertical walls. Compacting the material makes it more homogenous, making it easier to work with and easier for interpretation. The compaction also contributed to uniform mechanical properties in all the experiments. The difference in surface deformation is thus only controlled by the intrusion dynamics.

The cameras for surface monitoring (section 3.4), volumetric pump, and pressure gauge are connected to a trigger box. These are all connected to circuit board run by Arduino software that sends electrical impulses to allow for all the equipment to cooperate simultaneously. After the experiment, the trigger box is switched off, which stops the circuit. Images from the cameras are transferred to the computer and stored into folders that contain one picture from all the four cameras for each consecutive timestep.

3.4 The photogrammetric monitoring technique

To better understand the physical processes that govern the geological system, it is essential to quantify the results from laboratory modeling. Quantitative analyses of the laboratory experiments are done through the photogrammetric monitoring technique. The early methods of photogrammetric techniques and analyses were primarily limited in resolution and precision and were often overlooked by numerical models that were more advantageous at that time. Since that time, the techniques have steadily improved in accuracy and resolution, especially during the last few decades.

The monitoring techniques in this Thesis are developed by Galland et al. (2016). Data from the monitoring techniques are achieved by the use of Structure-from-Motion (SfM) photogrammetry (fig. 3.3). This is a monitoring method that uses MicMac algorithms. MicMac is a software package developed by the French National Geographical Institute (IGN) and is an acronym for "*Multi images par Methodes Automatiques de Correlation*". This is an open-source photogrammetric software that was primarily used for aerial mapping. The software processing allows for the production of digital elevation models (DEM) and orthoimages of the surface. DEMs show where the model surface rises or sinks. Orthoimages are a result of the surface from MicMac after correcting for distortion, camera tilt, and topographic relief. MicMac processes images based on four synchronized cameras recording simultaneous images at given time intervals. This means that each DEM and orthoimage is based on static snapshots of the surface at a given time. The principle of MicMac is that the user specifies functions that MicMac executes and specifies parameters for each function (Galland et al., 2016). For the experiments, we monitor the surface evolution with a time interval Δt=1 s. Creating DEM and orthoimages for each timestep gives room for a quantitative analysis of the model surface evolution. We infer that MicMac is a viable software for monitoring surface deformation. Such software can account for the relevance and complexity of intrusions in geodetic models, provide high temporal and spatial data, and test the robustness in geodetic models by integrating both surface and subsurface data (Galland et al., 2016).

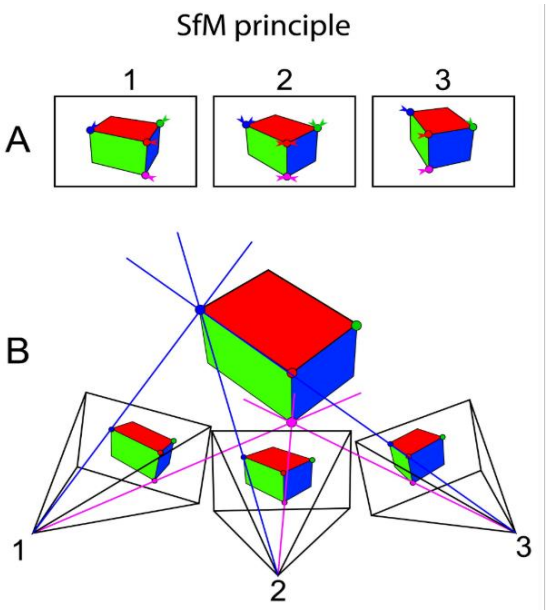

Figure 3.3: The principles of Structure from motion (SfM). Three cameras from different angles detect tie points (i.e., texture in the silica flour) and match them. (reprinted from Galland, et al. 2016).

3.4.1 The MicMac workflow

1. Several overlapping images are acquired from different positions.

2. The command "*Tapioca"* identifies for tie points in the images and assigned an identifier.

3. Common tie points in the set of images are then used to calculate camera positions, camera orientations and the distortion model with the command "*Tapas"*.

4. Evaluation of the preliminary model is done in a sparse 3D cloud with the position and orientation of the four cameras with the command "*Apericloud"*. This computes a ".ply" file, which can be visualized in *Meshlab* (or any other preferred 3D model visualization software. See figure 3.4).

5. GCPs are then used to scale and orientate the model, which transforms relative orientation to an absolute orientation. This is done by the command "*GCPBascule"*.

6. "*Campari"* is used to run the bundle adjustment, i.e., refine the camera orientation by compensation of heterogeneous measures, which are the tie points and the GCPs.

7. Information in the before-mentioned steps is utilized to create a digital elevation model (DEM) through digital image correlation with the command "*Malt"*.

8. Depth map is later calculated, combined with orthophotos, creating a high-density point cloud from "*Nuage2ply"*.

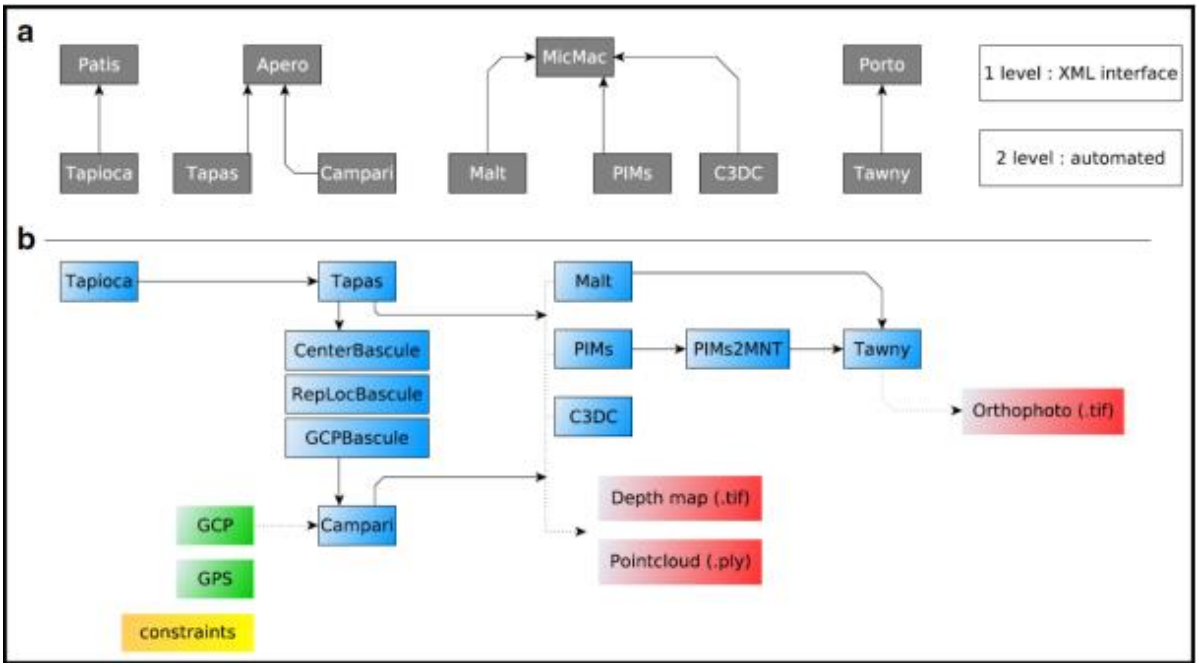

Figure 3.4: General MicMac architecture where the output data is marked in red, the commands are marked in blue, and the georeferencing inputs are marked in green (reprinted from Rupnik et al., 2017).

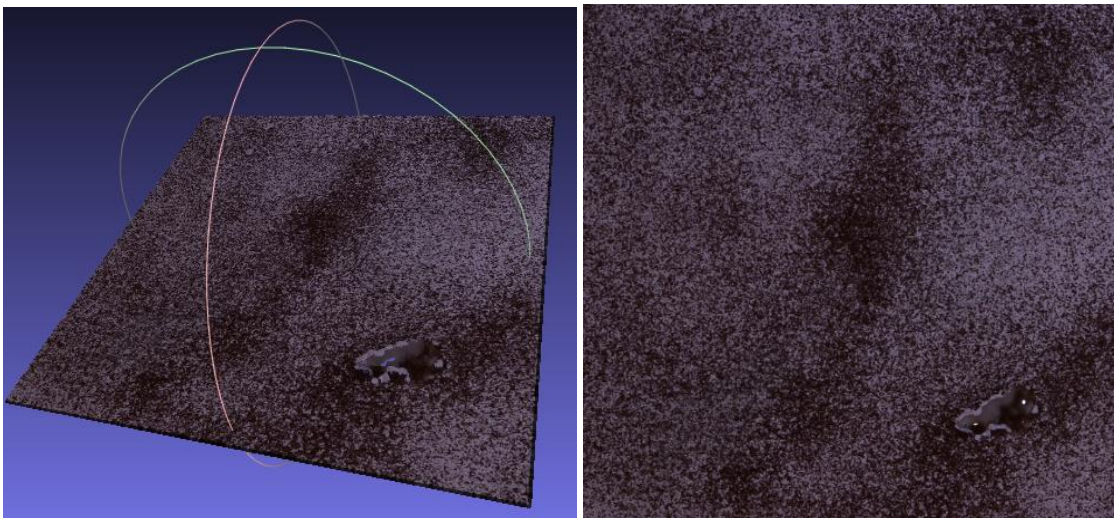

Figure 3.5: The left figure shows a high-density point cloud created from the DEM and the orthorectified image (left), which is a ".ply" file used for 3-D visualization. The right figure shows an

Orthorectified image of the model surface. Notice the dark spots on the model surface is the texture that allows MicMac to find and match tie points. The oil erupts at the right edge of the figures. Because of the transparent nature of the oil, it causes correlation difficulties in the affected area (see figure 3.6).

The homogenous host material produces a surface that has no points of reference for MicMac to process the photos. A well-textured model surface is important for MicMac to detect sufficient tie points between the pictures obtained from each camera. In order to create a well-textured surface, we apply coffee powder and olivine sand on the model surface. This produces sufficient information and overlap of each image. MicMac image correlation can be shown in the correlation maps in figure 3.6. With a textured surface, MicMac finds tie-points, which are points with the same location, in each image for each camera at a given time interval. This creates a relative orientation between the images and corrects the lens distortions.

Figure 3.6: Greyscale correlation map of the digital image correlation of the selected area of study. Darker shades correspond to poor correlation, and lighter shades correspond to good image correlation. Optimally these maps should be as white as possible. Notice the dark patch at the right edge of the figure. This is where the oil has erupted. The oil is transparent and reflective, which creates difficulties for the image correlation resulting in a bad correlation value.

During our setup, we use four cameras that are calibrated on the same spot and distance. Once each camera is calibrated, it is put to manual focus and put on their respective position above

the experimental cage. Camera 1 is located directly above the experiment, and the three others are located at a slight angle from the vertical. To enhance the images, we use several spotlights to produce proper lighting. Using four cameras focused on the same point, we can use the same distortion to all cameras during our experimental procedure. Four known ground control points are used in the model to convert from an arbitrary scale to a real-world scale. By synchronizing the cameras, we can compute high-resolution images of the surface at any given time interval.

The processing of the figures used in this Thesis is based on Matlab scripts that compute surface deformation of the monitored surfaces. Implementing Matlab for interpretation of our results allows us to generate visualized displacement plots that are derived from the previously explained MicMac software. This system provides computing high-resolution and high-precision maps of horizontal and vertical displacement maps of the surface deformation. Horizontal displacement maps can be used for producing shear strain and divergence plots. This allows for creating maps that show compressional and extensional fractures or faults. These scripts produce displacement maps with sub-millimeter accuracy (Galland et al., 2016). The maps allow for the generation of visual structural 3D models for quantitative monitoring of geological systems in the laboratory (fig. 3.7).

To visualize the models with photogrammetry, we need to combine the images from the four cameras. The cameras should be synchronized such that they shoot images of the surface evolution synchronously. All the cameras should have equal setting parameters. They should also have an angle of about 10-15 degrees (Galland et al., 2016), and be placed at a similar distance to the target model surface. The Structure-from-Motion principle consists of two main steps. (1): Detect and match tie points. This means that the software finds points with the same real-world location in different images. A tie point is a point where coordinates are not known, but the point is recognizable in at least two of the images due to the image overlap of a particular feature. The software detects pixels that show significant contrasts. It then describes these points and later combines points with similar descriptions in different images to create a feature point. (2): The second step involves the calculation of the relative positions of each camera. SfM uses different positions of the camera of homogenous feature points to calculate the relative position of the camera for each picture. An extensive set of feature points provide better results. Hence, it is essential that the object that is photographed has a visible and prominent texture. Viable texture material is olivine sand or black coffee because they are inhomogeneous and contains several distinct spots that can be evaluated by the cameras.

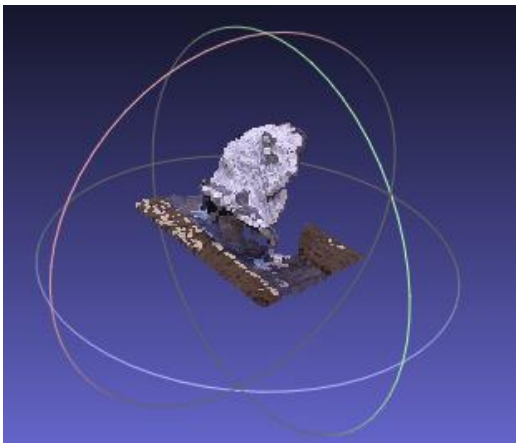

Figure 3.7: Example of a 3D computed model from the final intrusion geometry from one of our experiments. The image correlation in the 3D model suffers in regions that are not complete. This is because of bad images causing difficulties in computing comprehensive 3D models (See section 6.4 of a detailed explanation of factors that depend on 3D model computation accuracy).

Although a lot of surface monitoring techniques exist, none of them combines the advantages of low cost, high resolution, and precision, able to monitor topography and horizontal displacement and easy to setup. Our method, however, has these advantages (Galland et al., 2016). Our methods can also measure topographic changes and horizontal displacement maps in the same workflow. The calibration requirements are not very complex, and it can model surface deformation and internal structures. Our technique is consequently a viable method to construct the data acquisition obtained during this Thesis (limitations of photogrammetry are described in section 6.4).

3.5 Technical development

A significant role of this Thesis was the technical development to try to simulate laterally propagating dykes in a laboratory environment in a reproducible manner. Performing laboratory experiments involves creating physically valid experiments that can be reproduced by following the experimental procedure (see appendix A for complete experimental procedure). Prototyping an experimental design through countless failed experiments trying to simulate lateral propagating dykes has thus been a great part of this Thesis. Some experiments were repeated up to five times because of technical failures and to ensure reproducibility of successful experiments.

The experimental design is developed by Galland et al. (2006). Technical aspects of the experimental procedure were reworked to optimize the procedure during the evolution of this Thesis, with special emphasis on the volumetric tube system. We observed that the previously used tubes and clamps often did not withstand the driving pressure of the oil injection, which led to failed experiments. To overcome this, we changed most of the clamps and tubes and added slight changes to the system such that the end product was more time-efficient. Two different net types were tested and reworked in order to find an experimental procedure that allowed the net to be as rigid as possible such that the experiment could be confidently reproduced. To reproduce the experimental setup, the procedure needs to be followed carefully. Missing "minor" steps during the experimental approach led to invalid experimental results or complications in the data analysis (limitations are described in more detail in section 6.3).

Another major part of the Thesis involved in reworking the Matlab scripts to fit our experimental purpose. The code was already generated by the creators at the Physics of Geological Processes. However, we ran into countless of errors both in MicMac and Matlab during the process of fitting the code to our experimental approach. Reworking these scripts to fit our experimental purpose was thus a big part of the work. New scripts were also created to produce some of the plots shown in Chapter 4 (See Appendix C & D for scripts). Consequently, the experimental results can seem a bit on the short end side. However, we will try to show that the end-product of a successful experimental procedure, still can provide some valuable insights into magmatic processes and the associated surface deformation (if correctly scaled).

3.6 Scaling

Performing laboratory modeling has its advantages and disadvantages. The main advantage is the ability to simulate geological systems in a controlled manner within the laboratory. Conversely, performing such experiments introduces one of the major problems regarding laboratory modeling: Scaling. A big challenge for laboratory modeling is the vast difference in scale between the laboratory and the natural systems (Galland et al., 2018). This gap often leads to criticism regarding the validity of these experimental models. The word "scaling" has many different meanings, and the concept had a breakthrough during the 20th century, especially regarding the application of laboratory models.

Hubbert (1937) was the first to introduce the theory of scale models to the geoscientific community. This involved a change in consideration of the physical validity of analogue experiments. Hubbert said that laboratory models must fulfill geometrically, kinematically, and dynamically similarities to the natural counterpart (Hubbert, 1937). Geometrical scaling includes a ratio between nature and laboratory models. Kinematic scaling indicates a time scale and dynamic similarities include a ratio of forces and stresses (Galland et al., 2006). It is, therefore important to correctly scale the laboratory experiments with the natural systems to produce applicable model results (see table 3.1 for differences in our experiments and nature). However, there is still considerable confusion about the concept of scaling and the meaning of the word "scaling".

The confusion amongst scientists is related to the misunderstanding of what laboratory models are meant to reproduce. Laboratory experiments are not created to exactly mimic a geological system. Instead, they focus on understanding the physical processes and laws that govern the system, either individually or in combination. Experimental modeling is therefore a simplistic yet effective approach to gain valuable insights into the physical processes that govern a system. A great quote that arguably originated from Einstein stated that "*everything should be made as simple as possible, but not simpler*". In one way, understanding is the ability to ignore as much complexity from the physical system and distill a minimalistic experimental approach that describes the essence of such processes (Ben-Zion, 2017). However, a minimalistic approach might disturb the balance between the "realism" of the experiment and the physical applicability of the results.

It is essential that the material and experimental conditions are correctly scaled and are geometric, kinematic, and dynamically fulfilled. The geologically processes described by laboratory experiments can be reproduced in a manageable size with recordable timescales only if the material properties and dimensions are correctly scaled (Galland et al., 2006). Our experiments want to simulate the natural basin-scale phenomena. (Galland et al., 2009). Galland et al., 2006 stated that magma injection experiments in the brittle crust are correctly scaled if (i) the model crust has Coulomb failure criterion. (ii) The cohesion should be between 40 and 7500 Pa and has an angle of internal friction between 26° and 45°. (iii) Magma viscosity should be low (between 4×10^{-9} Pa s and 75 Pa s).

3.6.1 Dimensional analysis

To prove the applicability of the physical laws to geological systems, they should be dimensionless. This means that the laws are independent of length and time scales (Galland et al., 2018). Dimensional analysis is done to (i) provide dimensionless parameters governing the processes that are modeled and (ii) test similarities between laboratory experiments and the geological system we want to simulate. However, simulating magma injection in the brittle crust is still a challenge because of the large variety of magma viscosities and to properly scale both the magma dynamics and the deforming host rock (Galland et al., 2014). The goal is to find dimensionless numbers that can characterize geometry, kinematics and kinetics of the geological system.

Geometrical input variables from the dimensional analysis between experiments and nature are as follows: Depth (h) of the inlet, inlet diameter (d), injection velocity (v), density (ρ_m), viscosity (η), host rock density (ρ_r), internal friction angle (Φ) and cohesion (C). An external parameter is gravity (g), which is similar in both systems (Galland et al., 2014). We try to simulate a ratio where 1 cm in our experiments represents 1 km in nature (see table 3.1).

There are six dimensionless numbers ($\prod_{1\text{-}6}$) obtained from the variables above that characterize the physical system. Two of these (eq. 3.1, 3.2) define a geometrical ratio describing the coupling between magma and the host rock, which controls the formation of sheet intrusions (Galland et al., 2014). Equation 3.1 describes the ratio of geometrical depth-to-size. Experiments done by Galland et al., 2014 measured $\prod_1$ to span from 3 to 30 while dyke tips in nature span from 10-100,000. Equation 3.2 describes a dynamic ratio between viscous stresses from the magma and the strength of the host rock. Galland et al., 2014 found this value to span from 9×10^{-5} to 5×10^{-3} while the nature of dyke tips has a value of 10^{-7}-1. The four other dimensionless parameters play little role in our experimental interpretations because they involve host rock behavior ($\prod_3$, $\prod_4$) or magma flow ($\prod_5$) separately. The last dimensionless parameter ($\prod_6$) corresponds to magma buoyancy. In our experiments, we can control the velocity i.e., we can control buoyancy, which implies that this number is not important for our physical system (Galland et al., 2014).

$$\prod_1 = \frac{h}{d} \qquad \text{(eq. 3.1)}$$

$$\prod_2 = \frac{\eta v}{Cd} \qquad \text{(eq. 3.2)}$$

4 Results

4.1 Experimental results

The experimental procedure involved investigating the contribution of the net on the resulting surface deformation. To test this, we constructed experiments both with and without the net. In addition, we also conducted three different experiments varying the net depth parameter from 4 cm, 6 cm, and 8 cm. All experiments were repeated with the same foundation of parameters (some experiments were performed up to five times). This repetition was done due to failed experiments during our design testing and to ensure a sound experimental procedure with reasonable output data. The final experiments are listed in the table (4.1) below. The time steps provided in the figures correspond to the time in seconds allowing us to study the deformation pattern evolution. This section will include summarized results of the most representative and relevant maps for each of the experiments.

Table 4.1: Shows the experiments and their corresponding parameters.

Experiment	8 cm	6 cm	4 cm	Reference experiment
Net height (cm)	8 cm	6 cm	4 cm	-
Duration(s)	275	64	106	102
Silica flour mass (kg)	16	16	16	16
Compaction (kg/cm^3)	1050	1050	1059	1049
Horizontal/Vertical ratio	1,8	1,333	1,333	0,9
Injection velocity (mL/min)	30	30	30	30
T_{oil} (Celsius)	57	50	52	55

The experimental procedure allowed us to study the intrusion characteristics of the solidified intrusion after the experiment. Figure 4.1 shows the final intrusion body produced from our

experiment with an 8 cm net. It is a thin sub-vertical sheet with an irregular outline. Central regions of the intrusion contain small protrusions, while the main sheet wall is smoother at the edges. The outline of the net is observed at the edges of the intrusion. On top, there is an oblique sheet of erupted oil. The intrusion has a maximum vertical extent and a maximum height of 18 cm and 10 cm, respectively, which corresponds to a final aspect ratio of 1.8:1.

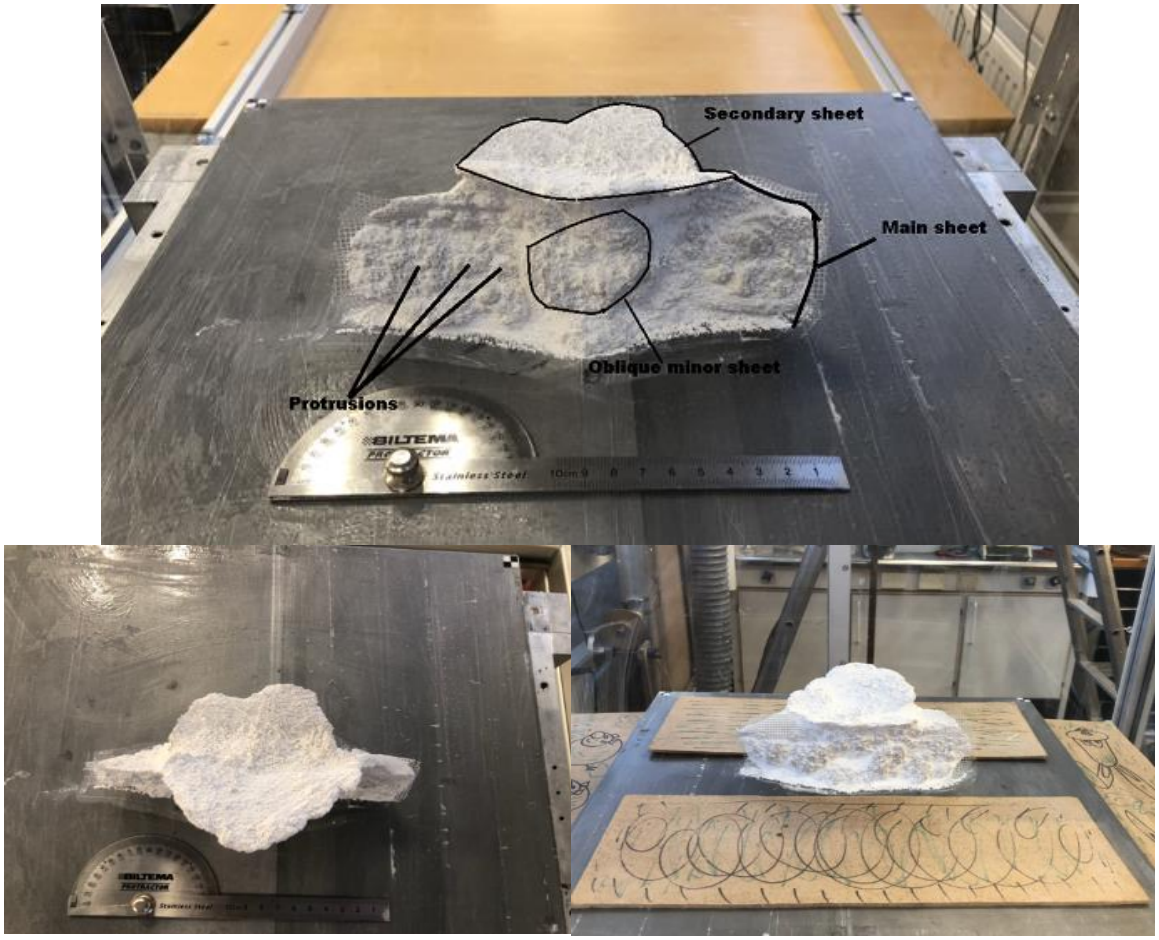

Figure 4.1: Examples of the final geometry of an excavated intrusion using an 8 cm net. Intrusion characteristics are outlined and marked in the upper image. The lower left is a top view, and the lower right is the back view.

The first experiment was performed without a net to get a general idea of dyke emplacement and the surface deformation, which is later compared to experiments using a meshed net of various heights. This experiment will show the expected surface deformation produced simply by only injecting magma into the crust. An important note is that one experiment is by far not sufficient to describe the behavior of magma injected into a cohesive Coulomb host, but rather

give slight insights into the relative contribution with and without the net as a propagation contributor.

4.2 Experiment without a net

Results obtained from the experiment with no net is described in figure 4.2. The duration of the experiment lasted for 102 seconds. Figure 4.2.1 shows displacement maps in the horizontal U_x-direction with 30 seconds timestep intervals. These maps show surface displacement parallel to the x-axis. Positive values (red) indicate displacement towards the east and negative (blue) indicate values towards the west. The displacement field seems to develop in a relatively symmetrical pattern throughout the experiment (A, B, C). The negative displacement covers a larger area, but the magnitude of the positive and negative displacements is about the same (C). As the experiment evolves, the displacement grows towards the north. The displacement field seems to divide into subsections that are defined by lines that differentiate higher displacement contrasts. These lines correspond to fractures that form during the ascend of the magma through the silica flour. The evolution of brittle deformation can be studied in divergence maps. Note the artificial stripes in our U_x and divergence maps that seem to grow as the values increase (see section 6.5 for a discussion of these artifacts).

The divergence plots are shown in figure 4.2.2 (A, B, C). Divergence is a vector field that measures a scalar value of how the vectors in the field are diverging or converging, i.e., the expansion or compaction at a given point. If the field is expanding, the divergence of the field is positive. If the field is compressed, the divergence of the field is negative. Positive values indicate stretching, and negative values indicate shortening. These plots are derived from the horizontal displacement "U_x" and the vertical displacement "U_y". These divergence maps show the compressional and extensional zones or surface fractures caused by the uplift during the evolution of the experiment. Throughout the experiment, two major extensional fractures seem to develop going in the NS direction. At the later stages of the experiment, minor extensional fractures develop, striking in the EW direction (B, C). A circular region of compressional fractures defines the outer rims of the deformed area (C).

ΔDEM maps are shown in figure 4.2.3. These maps indicate the topographic difference from the initial surface (A, B, C). These maps show the elevation and subsidence of the experimental model surface. DEM maps produce insights in where the topography rises or sinks, the

magnitude, and area of the elevation change. Positive values show surface elevation, and negative values correspond to subsidence. Throughout the evolution of the experiment, the digital elevation models produce overall surface elevation only. The elevation generally increases in magnitude proportional to the time (although this is not the case for the early stage) and is confined within a sub-circular area. The highest value of surface elevation of the final time step indicates the eruption point of the experiment (C).

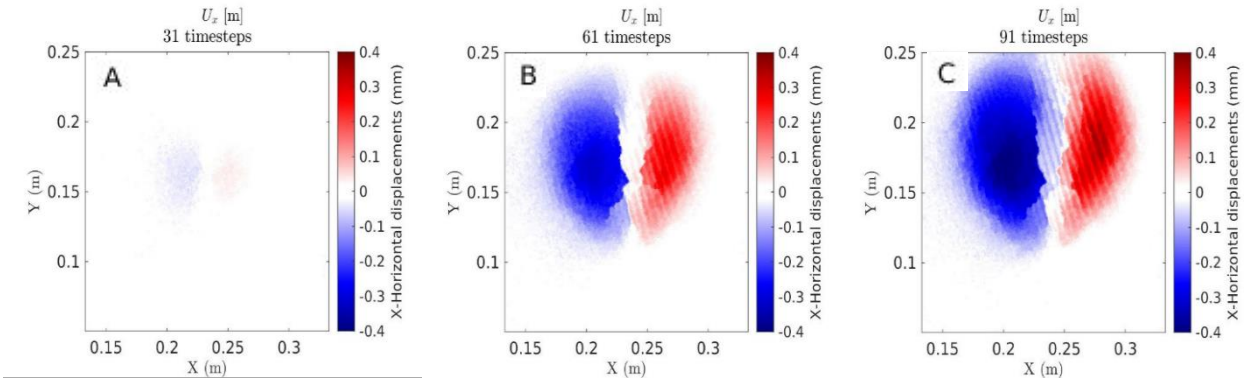

Figure 4.2.1: Shows results from the reference experiment with no net. The figure shows incremental displacement maps for in the X-direction for time step 31 (A), 61 (B), and 91 (C). Positive values indicate displacement towards east and negative values indicate displacement towards the west.

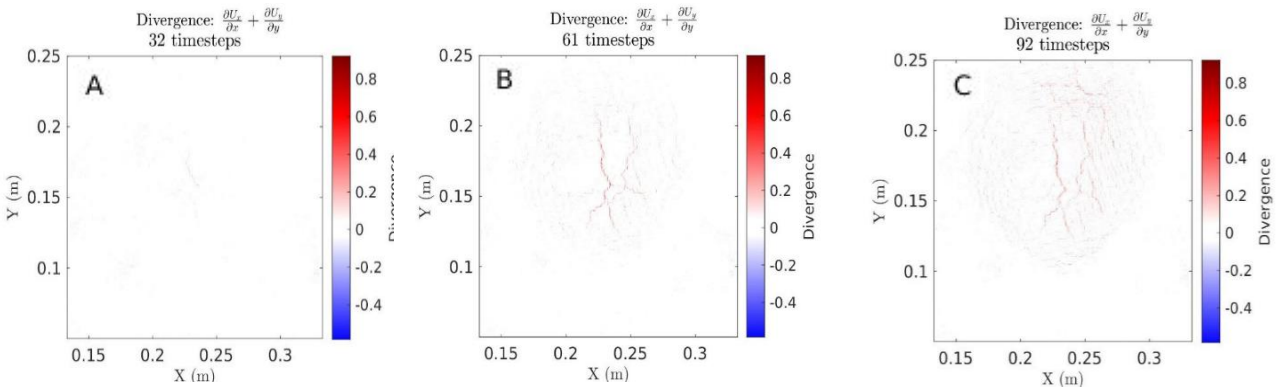

Figure 4.2.2: The figure shows the divergence field from time step 32 (A), 61 (B), and 92 (C). Positive divergence (red) indicates extensional regimes, negative divergence (blue) indicate compressional regimes.

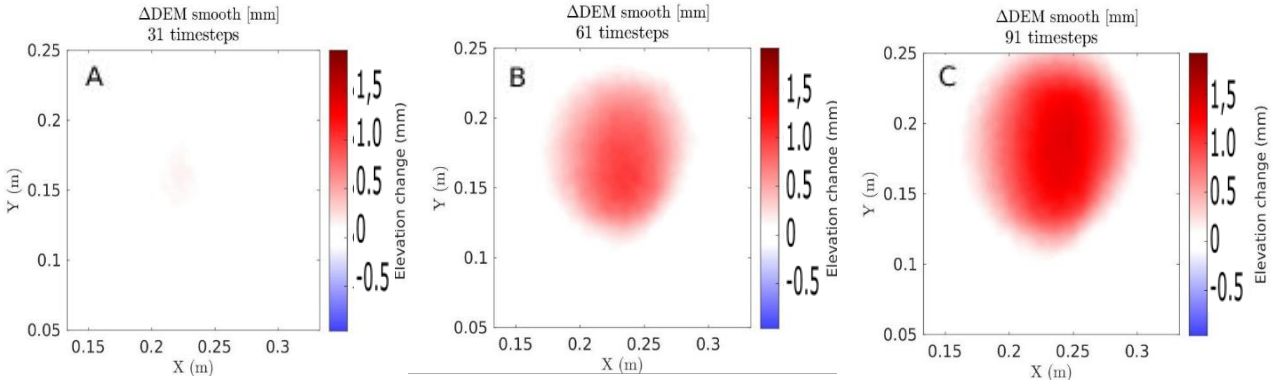

Figure 4.2.3: The figure shows ΔDEM, indicating a topographic difference from the initial surface for time step 31 (A), 61 (B), and 91 (C). Positive values indicate surface elevation, and negative values indicate subsidence.

4.3 Experiment 8 cm net height

The results obtained from the experiment with an 8 cm net are summarized in figure 4.3. The horizontal displacement is shown in figure 4.3.1. The orientation of the net is shown in figure (A) and held constant throughout the experiments. The U_x maps show that the horizontal displacement develops in a symmetrical pattern, most notably in the early stages (A, B). The horizontal displacement pattern grows southwards as time increases. The divergence field (figure 4.3.2), in the initial stages (B) forms two sets of extensional fractures in the east-west direction aligned parallel to the net. These grow until the later stages (C), where another set of extensional fractures develop in the NS direction. The outer rims are defined by a circular compressional region, which has the highest magnitude at the southern part where the oil breaches the surface (see also 4.3.3 (C)). The digital elevation (figure 4.3.3) model shows only surface elevation. The area of surface uplift is circular with an increasing magnitude as time evolves and towards the rupture point. The rupture point has the highest surface elevation and is marked by the star (C).

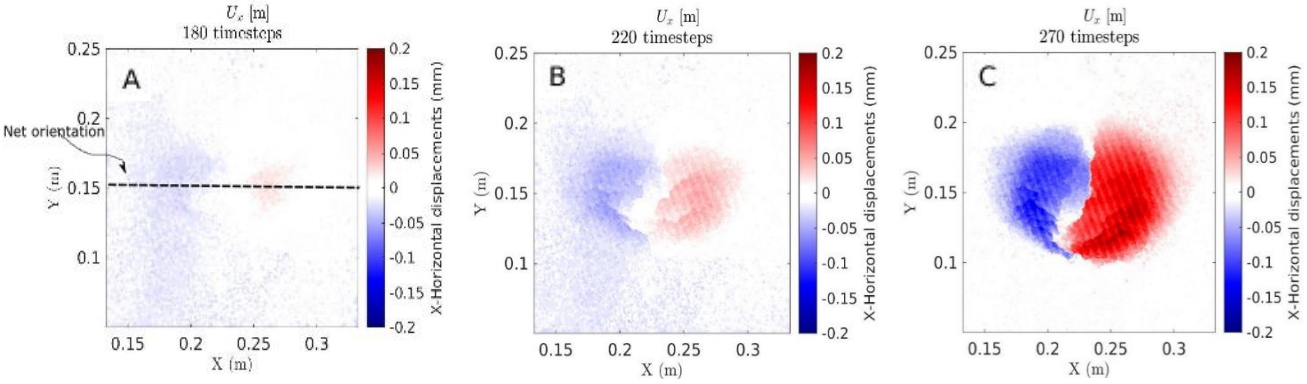

Figure 4.3.1: Shows results from the reference experiment using an 8 cm net aligned in the middle striking in the east-west direction (A). The figure shows incremental displacement maps for in the X-direction for time step 180 (A), 220 (B), and 270 (C). Positive values indicate displacement towards east and negative values indicate displacement towards the west.

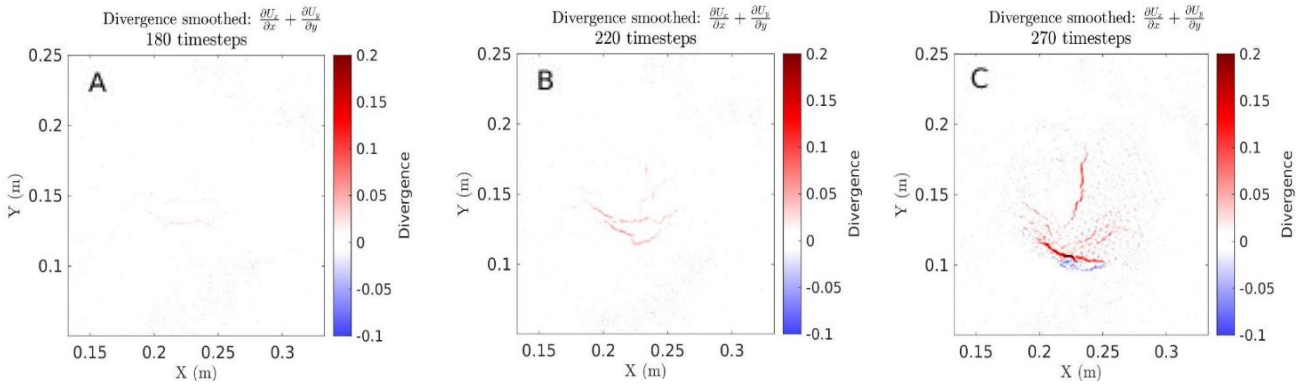

Figure 4.3.2: The figure shows the divergence field from the experiment using an 8 cm net from time step 180 (A), 220 (B), and 270 (C). Positive divergence (red) indicates extensional regimes, negative divergence (blue) indicate compressional regimes.

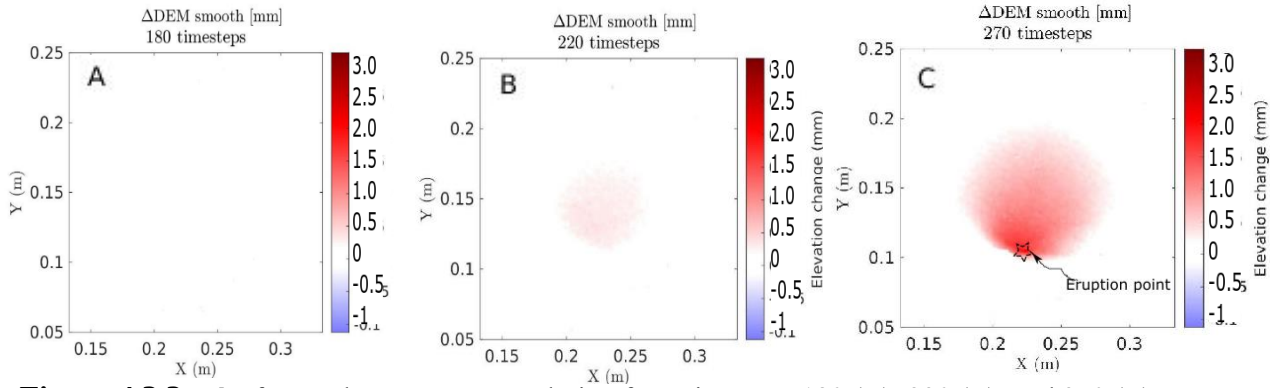

Figure 4.3.3: The figure shows ΔDEM evolution from time step 180 (A), 220 (B), and 270 (C). Positive values indicate surface elevation, and negative values indicate subsidence. The time step corresponds to the time in seconds. The eruption point is located by the star (C).

4.4 Experiment 6 cm net height

Experiment 6 shows a symmetrical pattern in the evolution of horizontal displacement in the first stage (fig. 4.4.1 A-B). The displacement firstly grows centrally, followed by growth towards the south. At the final stage (C), the areal extent of the displacement field gets smaller towards the eruption point. The divergence field shows a “three-armed” set of extension fractures that grow parallel to the net and one arm going perpendicular (fig 4.4.2 A-B). At time step 38, the extensional fractures evolve downwards, and the outer rim of compressional fractures starts to develop. Little surface elevation is shown in the early stages of the intrusion demonstrated in figure 4.4.3 (A). The uplifted region is accelerated simultaneously with the formation of the downwards forming extensional fractures.

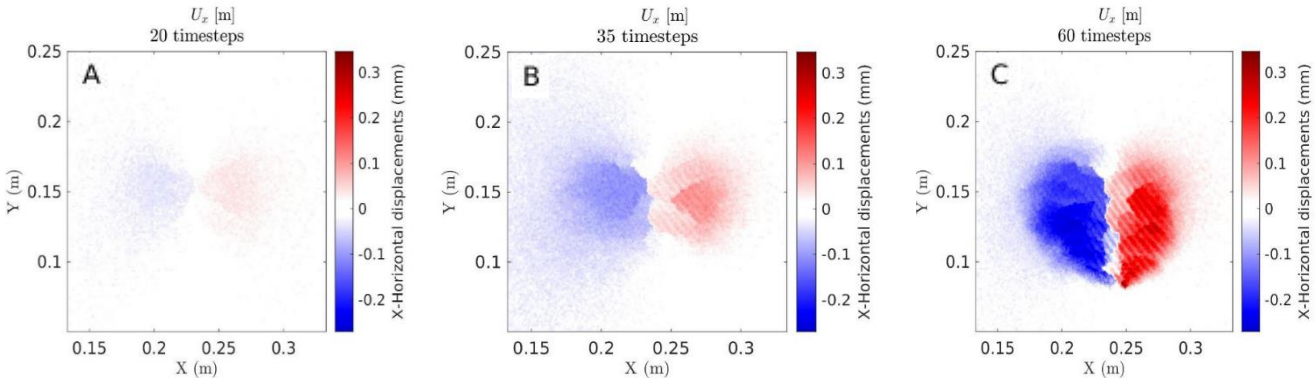

Figure 4.4.1: The figure shows U_x displacement from the experiment with a 6 cm net. Positive values indicate displacement towards east and negative values indicate displacement towards west. From timestep 20 (A), 35 (B) and 60 (C).

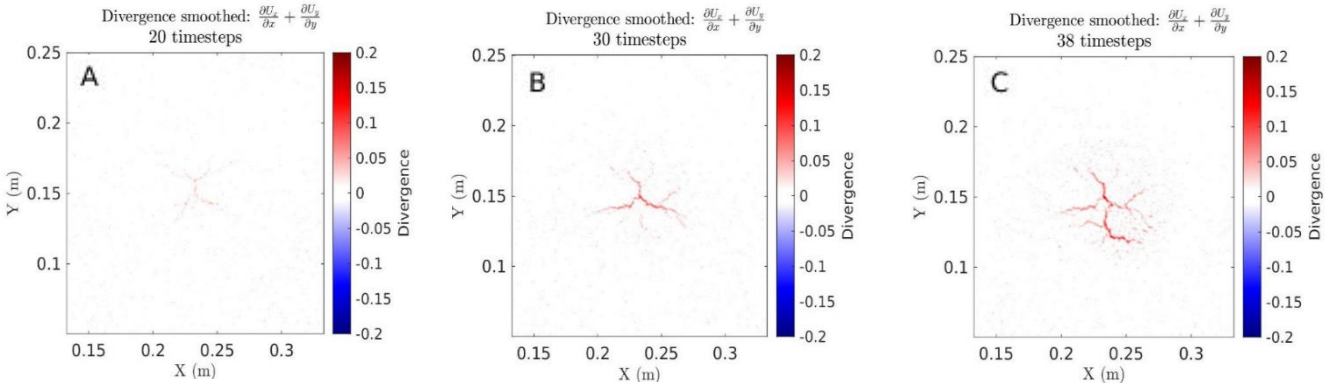

Figure 4.4.2: Shows divergence field from the experiment with a 6 cm net. From time step 20 (A), 30 (B), and 38 (C).

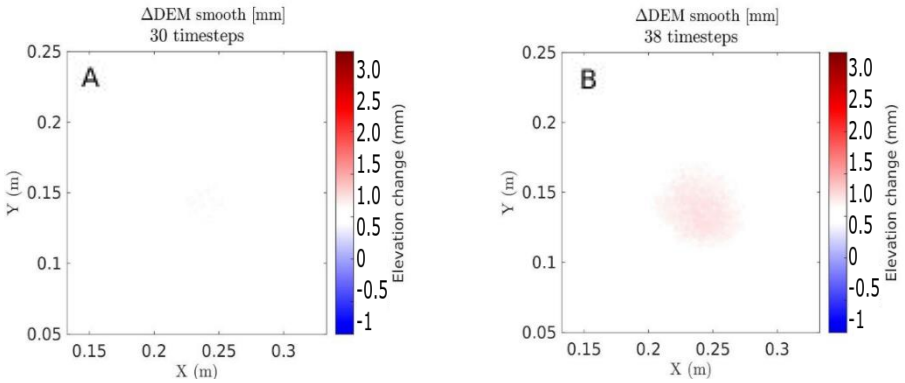

Figure 4.4.3: Shows digital elevation for the experiment with a 6 cm net with timestep 30 (A) and 38 (B).

4.5 Experiment 4 cm net height

Figure 4.5 summarizes the results from the experiment with a 4 cm net. Initially, the horizontal displacement seems to be symmetrical (A). As time evolves, the displacement becomes asymmetrical, with negative horizontal displacement dominating over a larger area (fig. 4.5.1 B, C). The divergence maps initially show a “three-armed” radial set of extensional fractures (A). These radial “three-armed” extensional fractures evolve towards the southeastern corner with two sets striking in the east-west and north-south direction at the final stages (C). The outer rims are defined by a circular compression region with the highest magnitude at the southeastern part where the oil breaches the surface (C). The digital elevation model shows a symmetrical circle at the initial stages (A, B). At the later stages, the surface elevation increases towards the south-east. The eruption point is marked by the star (C). The overpressure evolution as a function of time is shown in figure 4.5.4. The pressure shows a low-pressure stage, followed by a rapid pressure increase until it reaches the maximum overpressure. After this stage, the pressure levels steadily decrease over the experiment duration.

Figure 4.6 depicts maximum values of the DEMs as a function of time T (s) for experiment 6 cm (blue), 8 cm (red), and 4 cm (black). A general trend for the experiments with a net show low values of maximum DEM at the early stages of the experiments. Later, the figure shows a rapid acceleration of maximum DEM values in short time intervals.

Plots of DEM versus a transect parallel to the aligned net in the X-axis for experiment with net (left) and without a net (right) is shown in figure 4.7. The figure shows incremental time steps of 10 seconds from the bottom line to the top. Notice the broader extent of surface uplift generated from the experiments with a 4 cm net (left) compared to the experiment without a net (right).

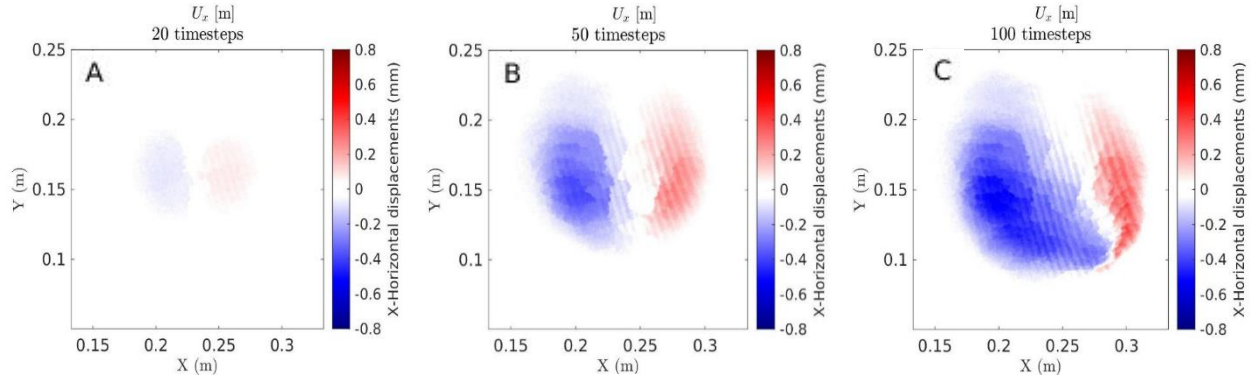

Figure 4.5.1: The figure shows results from the experiment using a 4 cm net (A-C). The left column shows displacement maps for in the X-direction. Positive values indicate displacement towards east and negative values indicate displacement towards the west.

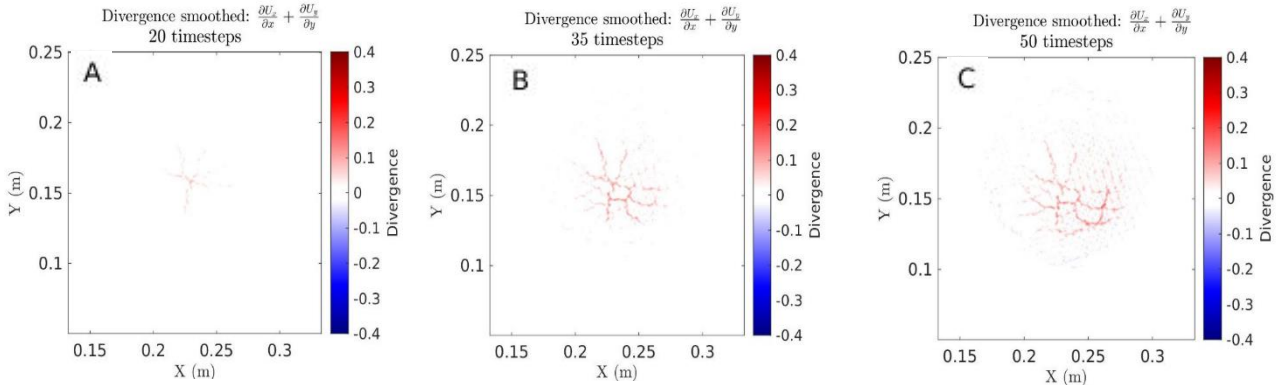

Figure 4.5.2: The figure shows the divergence field. Positive divergence (red) indicates extensional regimes, negative divergence (blue) indicate compressional regimes from time step 20 (A), 35 (B), and 50 (C)

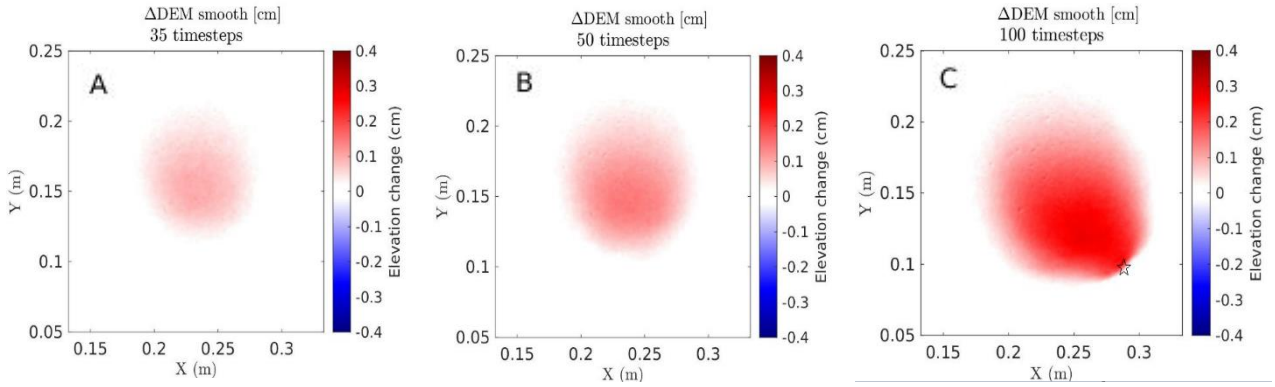

Figure 4.5.3: The figure shows ΔDEM from time step 35 (A), 50 (B), and 100 (C). Positive values indicate surface elevation, and negative values indicate subsidence. The time step corresponds to the time in seconds. The eruption point is located by the star (C).

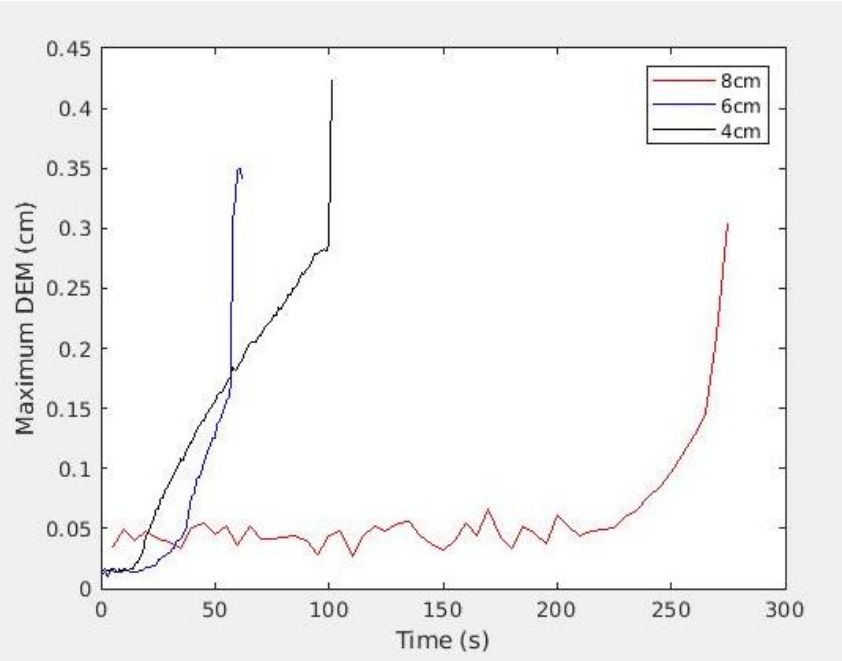

Figure 4.6: Plots of maximum values of the DEMs as a function of time T (s) for experiment 6 cm (blue), 8 cm (red), and 4 cm (black).

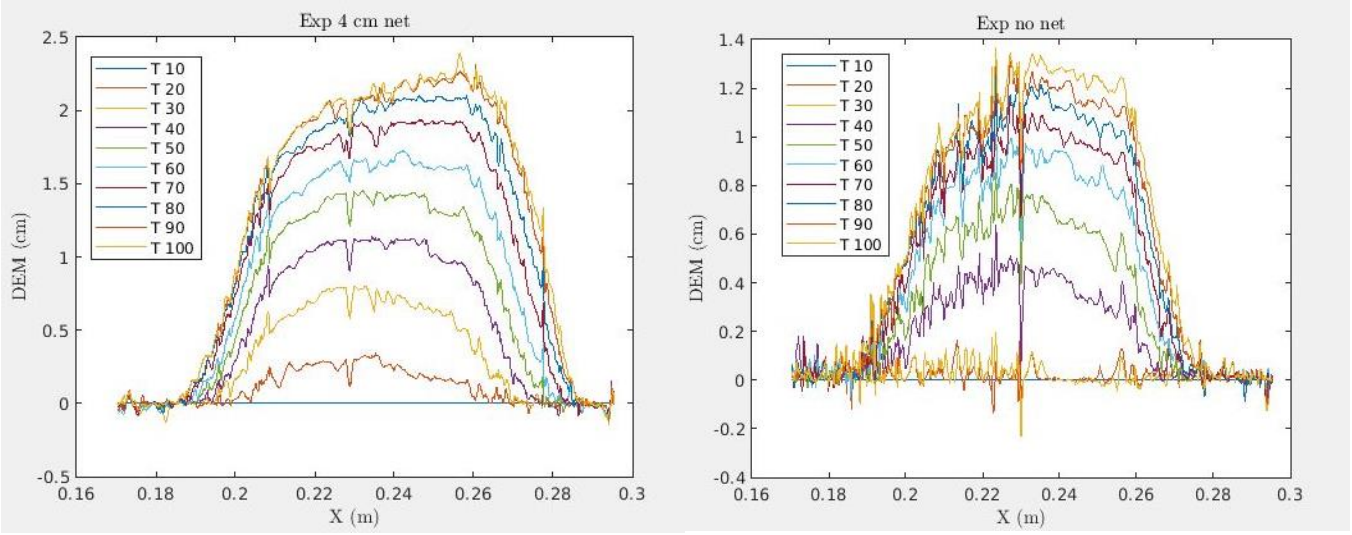

Figure 4.7: Plots of DEM versus a transect parallel to the aligned net in the X-axis for experiment with net (left) and without a net (right) for incremental time steps of 10 seconds from the bottom line to the top.

5 Interpretation

In this following chapter, we will provide an interpretation of our experimental results and the effect a meshed net imposes on lateral dyke propagation and the associated surface deformation. We aim to highlight the similarities and differences between the experiments. One of the differences is shown in the horizontal displacement maps. The experiments with a net exhibit an "elliptical" areal extent, wherein the largest area aligns parallel to the net. However, the experiment with a 4 cm net height depicts an asymmetrical displacement pattern at the later stages dominated by displacement in the negative x-direction. The reference experiment, on the contrary to the aforementioned, has the smallest areal extent in the central region that progresses upwards towards the eruption point. We infer that the difference observed in these maps are caused by lateral magma propagation resulting in a larger central field of displacement in the experiments with the net.

The divergence maps produced in the reference experiment show north-south striking extensional fractures developing in the early stages (fig. 4.2.2). The divergence maps in the experiments that are affected by the net portray dominating east-west striking extensional fractures in the early stages. At later stages, more fractures develop, generally striking in the north-south direction. The fracture pattern appears to be defined by extensional fractures that form at the dyke apex. Similarities in the divergence field maps between the experiments are the compressional fractures at the outer rims produced in the later stages of each experiment.

A similarity in all the experiments is the apparent symmetrical sub-circular uplift pattern produced by the DEMs. All experiments including a net follow this pattern. The reference experiment is however more "balloon" shaped and has the highest magnitude of surface uplift in the central region. The other experiments have the highest magnitude of surface uplift at the edge of the uplifted area. Their overall shape is broader in the central region, whereas for the reference experiment, the areal extent in the central region is the smallest. An interesting observation is the delayed onset of surface deformation in experiment 8 cm. The duration of this experiment was by far the longest with a duration of 280 s. Here, surface uplift is barely visible after 220s, implying a delayed onset of observed surface deformation. It would be reasonable to assume that the surface volume uplift volume is directly proportional to the injected volume. However, this is not the case for experiments performed by Guldstrand et al.

(2017) & Bertelsen et al. (2019) who in similar experiments measured a low ratio of uplifted volume to injected volume, suggested to be a product of compressible deformation of the host rock accommodated by the dyke.

The early stages of the DEMs generally show low amplitudes of surface uplift (see fig. 4.4.3). At these early stages, extensional fractures dominate parallel to the aligned net. Once the extensional fractures start to develop in a north-south direction in the later stages, the magnitude of surface uplift appears to accelerate in correlation to the newly formed extensional fractures. We infer that the emplacement mechanisms in our experiments with a net can be interpreted as a two-stage evolution (fig. 4.6). In the first stage, the dyke propagates along with the net in a deep, high confinement setting where dyke widening is favorable. The emplacement of the dyke tip can be expected to propagate in such a manner that the total potential of the system is at a minimum. Equivalently, the emplacement of the dyke tip should be favored in a way that it allows for the greatest energy release. In other words, the emplacement of a dyke is expected to travel the path of least resistance and is governed by the orientation of the least compressive stress (σ_3) (Heimisson, 2015). At this stage, the dyke propagates deep within the crust, resulting in a low amplitude uplift. We infer that the uplifted volume at deep levels is significantly less than the injected volume of oil due to the high overburden pressure and plastic deformation (see section 6.1), resulting in small magnitudes of surface uplift. In the second stage, the dyke starts to interact with the free surface, and the forward pushing behavior is favored, resulting in acceleration towards the surface. The upwards propagation requires less force to displace the overburden than the force required to displace the material in front of it. This is also shown in figure 4.6, which illustrates plots of maximum values of the DEMs as a function of time T(s) for 8 cm, 6 cm and 4 cm experiments. All experiments show low values of maximum digital elevation at one stage, followed by a rapid acceleration defined in stage two. Consequently, we infer that the emplacement mechanism appears as a crucial parameter to interpret surface deformation data in volcanic rifts. This feature is often overlooked, signifying the importance and diversification of such results.

The stark contrasts between the reference experiment and the experiments with a net give confidence in using the net experimental parameter as a contributor to dyke propagation. Hence, the experimental data of surface deformation can be applied with greater confidence when we attempt to understand associated surface deformation in volcanic environments. In the following chapter, we will discuss the implications this imposes for interpreting geodetic data and the limitations related to our experimental design and results.

6 Discussion

6.1 Emplacement mechanisms of dyke propagation

Surface deformation as a result of dyke emplacement has been studied in the laboratory, in theoretical models and the field. Mastin & Pollard (1988) pioneered dyke related surface deformation in the laboratory. Here they used a 2D cell filled with cohesive flour and modeled the dyke by insertion of sheets. Trippanera et al. (2014) later did this in three dimensions providing laboratory results of trough above the dyke tip and surface elevation on the margins of the trough as the dyke widens. The subsidence in the laboratory experiments is accommodated by central depression, with normal faults that bound the trough. This is in good agreement with theoretical models from Polard & Holzhausen (1979) of a tensile dyke emplacing in an elastic medium, as well as geodetic and field data from e.g., Pallister et al. (2010). The laboratory experiments of Trippinaera et al. (2014) and Mastin & Pollard (1988) correspond to analytical models of an inflating dyke (Galland et al. 2018).

Surface deformation observed in our experiments is generated by surface elevation along the zone of the subsurface dyke where the highest elevation is just below the apex of the underlying dyke. The fracture patterns are also defined by extensional fractures at the dyke apex and compressional regimes at the rims. We infer that this pattern is due to the forward pushing behavior of igneous intrusions, which concord with field observations from Cuesta del Chihuido (Spacapan, 2016). The host rock comprises marine laminated sediments and reverse faults, folds, and imbricate structures in order to accommodate a series of sheet intrusions and a dyke (Figure 6.1). The intrusions evince rounded, blunt, or rectangular tips combined with the brittle and ductile shortening of the host rock. The host rock deforms in a plastic manner, which is also supported by laboratory models (e.g., Abdelmalak et al., 2012; Guldstrand et al., 2017; Galland et al., 2009; Galland et al., 2012; Bertelsen et al., 2019). Thus, indicating the forceful “pushing” nature of dyke head propagation during the earlier stages of dyke evolution known as the viscous indenter model. The associated deformation caused by the viscous indenter model is restricted to a small domain called the “process zone”, in which the size is negligible with respect to the scale of dykes. This implies that the emplacement mechanisms correspond to how the host rock responds predominantly through plastic deformation to dyke propagation and that the energy is dissipated through the fracturing of the silica flour. This

emplacement mechanism produces distinct surface deformation (fig. 2.16) compared to the commonly assumed tensile fracturing accommodated by elastic host rock deformation.

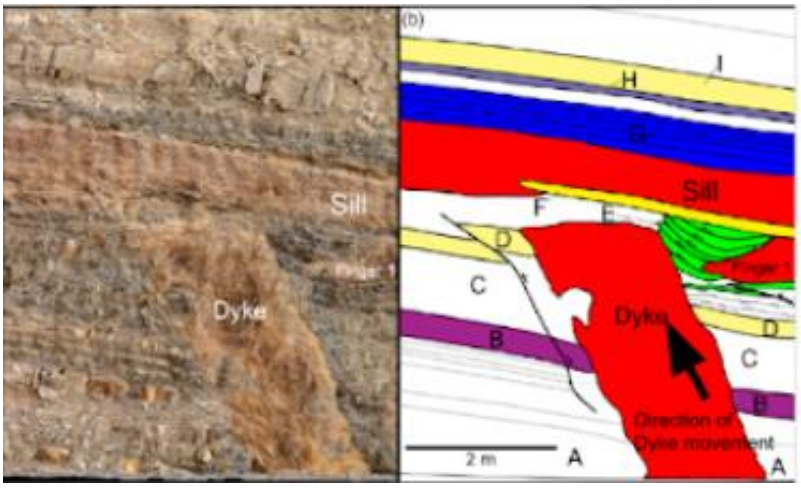

Figure 6.1: Shows field observations from the Cuesta del Chihuido outcrop. The right side shows sill, dyke, and finger intrusions. Deformation shows a reverse fault to the left of the dyke and imbricate structures to the right. The direction of dyke movement is shown by the arrow (reprinted from Spacapan, 2016).

6.2 Implications for geodesy

Insights into the relationship between surface deformation and the subsurface processes are implemented through analytical models of source deformation (e.g., Okada, 1985; Mogi, 1958). The linkage between surface deformation and the subsurface processes has been modeled both analytically and numerically. Geodetic models calculate surface deformation from a source with known parameters such as position, shape, and kinematics to fit the observed surface deformation with a plausible deformation source. The best fit represents the model that adequately reproduces the observed surface deformation. However, geodetic models suffer from a wide range of limitations. These models often assume deformation sources that are not documented as geological evidence. In essence, by modeling too simplistic intrusions, it implies that they might be physically unfeasible.

Our cohesive coulomb experiments produced only surface uplift, contradicting the two lobes separated by a trough calculated in geodetic models accounting for dyke opening (e.g., Okada, 1985). Geodetic models representing only surface uplift signals are described in the Mogi (1958) model, which models an inflating finite spherical source and inflating horizontal sills by

Okada (1985). However, these geodetic models are simplistic mechanical models that are based on the following assumptions: (1) Dykes open in a purely elastic, isotropic half-space. (2) There are no tectonic stress boundary conditions, and (3) the models occur as static deformation (Okada 1985). These models describe the simplistic processes of the emplacement of a magma volume with an idealized geometry with uniform properties surrounded by a homogenous host rock (Sigmundsson et al., 2018). It implies that they do not account for propagation mechanisms or mechanical properties, which are essential parameters to provide a sound physical interpretation.

Furthermore, several models often focus on the elastic response of the host rock but do not account for the plastic deformation such as faulting. Plastic deformation arguably plays a significant role in nature, most notably in rift zones (Galland et al., 2012). Geodetic models also do not take into account the complexity of volcanoes such as topography, mechanical heterogeneity, and regional tectonic deformation. Field observations from (Gudmundsson, 1983) show that the dykes are focused in a small area and show host rock in between. The natural complexity of such processes is challenging to simulate in simplistic models highlighting a caution on fitting such models. These statements challenge the applicability of these models based on the conditions of our laboratory experiments. Geodetic models assume end-member rheology, such as linear elastic behavior in an isotropic half-space. Thus they are of limited constrain under conditions in which the dykes form. In reality, Earth's crust exhibit both elastic and plastic behavior. Our experiments, however, are not confined to these assumptions and exhibit elastic and plastic behavior, and the boundary conditions are defined from the experimental box. The oversimplification of interaction between host rock and magma mechanisms in geodetic models might interfere with the physical relevance of such models.

Caution should therefore be applied when surface uplift signals are fitted with geodetic models that only calculate surface uplift due to how the deformation source geometry and physical mechanisms would be inadequate. Our experiments simulating lateral dyke propagation emphasizes the importance of the emplacement mechanisms, which produces different surface deformation then expected from the geodetic models. This implies a caution to the choice of physically relevant models to achieve a sound interpretation of geodetic signals.

Geodetic models are simplistic mechanical models that are based on assumptions that are too rudimentary. Geodetic models should also include errors of the used parameters. Physically complete models for numerical and geodetic models are difficult to create due to the complexity

of Earth's heterogeneity and the computational impracticality of including all aspects of dyke propagation. All data inversion must be carefully chosen, and a correct fit with geodetic models and experimental models does not indicate a physical relevant interpretation. This might call for a consideration of new developments in more physically relevant analytical models that will offer better interpretations of geodetic data.

6.3 Experimental limitations

Performing simplistic laboratory experiments can be a fun and unique way of investigating the processes that govern the geological system. However, such an approach introduces many limitations with regard to experimental modeling. This procedure is highly dependent on a consistent setup procedure done by the scientist performing them. Inconsistencies within the experimental setup procedure can cause the propagation of magma to flow in very unexpected ways, which in turn will result in a surface deformation that might be difficult to interpret. A plausible example of this is during the setup of the net at the start of our experiments. Optimally, the net should be very rigid and vertical, and it should not be readjusted during the experimental procedure. This was arguably the most difficult part of the experimental procedure, as pouring flour into the box will, in some way or another, affect the initial position of the net. The non-opaque silica flour also makes it difficult to observe whether the net is rigid or has shifted from its original position above the inlet. A shift in the net's position could potentially impact the desired "connection" between the magma and the meshed net. Hence, it is crucial to be consistent with the setup and try to keep the procedure as consistent as possible throughout all the experiments.

Another major limitation is the preparation of the model surface. Galland et al. (2014) found that DEMs are highly dependent on the model preparation procedure. Especially with emphasis on the model surface and the texture. Insufficient model surface texture density yields too few tie points, which again affects the image correlation. Consequently, the resulting models will be weak. A proper model preparation procedure is, therefore, essential for optimal photogrammetric results. If the texture is lacking, the resulting output data can become noisy or provide insufficient output data. The intensity of the noise can be due to low surface deformation or troublesome processing during the image correlation because of inadequate (or too much) texture coverage. Additionally, the oil erupting the surface at the end of the

experiment is transparent. Transparent materials will produce calculation errors when the oil has breached the surface. This will however only affect the very last part of the experiment, which is not particularly relevant for our scope.

Furthermore, the setup does not take into consideration topography and heterogeneity, which is an essential aspect of Earth's complexity. The initial surface of our experiment was flat and contained within a homogeneous medium. Our models simulate ideal isotropic conditions. Any pre-existing fractures, layering, and stress barriers that could influence the stress pattern induced by the intrusion is beyond the scope of this thesis. The complexity of nature is not simplified in such conditions as equivalent to our experiments. The complexity of Earth is with the current experimental setup, still a difficult issue to overcome.

6.4 Uncertainties of the photogrammetric method

The accuracy of the produced photogrammetric models relies on several factors. It is dependent on the level of image correlation between the images. This can be portrayed in the correlation maps produced by MicMac (fig. 3.6). Correlation maps that are produced from low correlation values that give rise to dark regions as a result of image correlation caused by too few tie-points. A poor correlation could reflect areas with little contrast or if the area is reflective, transparent, or if the model surface has a monotone coloring and contains topography that creates shadow zones. It indicates that the resulting figures produced from the photogrammetric method are heavily dependent on the experimental procedures, and most notably the way texture is applied to the model surface you want to photograph. It is crucial to provide sufficient texture with neither too little nor too much texture to the model surface so that MicMac can find enough tie-points to produce adequate correlation maps.

Photogrammetric model uncertainties are also dependent on systematic and planning errors. Systematic errors are due to camera systems. In essence, lens distortions, principal distances, and the resolution of the images. The resolution is an essential factor as it is governed by the camera's focal length and sensor size. Lens distortion is also important because it makes points on images plane shift from its original to a new position (Dong-Hyun, 2016). Planning errors is related to the camera network geometry, meaning the camera positions and object position (Dong-Hyun, 2016). Factors that control planning errors are baseline distances, an overlap of images, and angle of incidence. When constructing 3D models, depth accuracy is dependent on

the base-distance ratio, with accuracy increasing with increasing distance from the camera to the targeted object (Dong-Hyun, 2016). However, increasing the distance of the camera can make common tie-points recognition troublesome.

Ideally, images from the four cameras should have at least a 60 percent overlap. These images should be balanced by image density and processing time. Optimal images are governed by the angle of incidence, which is the angle between the optical axes of the lens and the line perpendicular to the surface. This angle should be as low as possible. Moreover, the angle should be adjusted when constructing 3D models to prevent shadow zones in the object geometry that infer with the 3D models (Dai et al., 2014). Constructing photogrammetric models is reliant on many factors, that in turn can affect the results produced from such models. Hence, it is important to test these factors and create a photogrammetric system that is optimized for the experimental procedure we want to perform in the laboratory.

Table 6.1: Depicts how photogrammetric parameters affect the accuracy of the method.

Factor	**Level of accuracy**
Distance	Closer distance, higher accuracy
Overlapped images	More overlapped images, higher accuracy
Intersection angle	Closer to 90 degrees, higher accuracy
Angle of incidence	Closer to 0 degrees, higher accuracy
Resolution	High resolution is highly correlated with accuracy
Features	More features and more colors, higher accuracy

6.5 Artifacts produced in the displacement maps

Relying on MicMac for image processing and a consistent setup procedure can also play a role in the outcome obtained from the image processing. A noteworthy observation in our results is the artifacts produced in our displacement maps that are predominantly observable in the Ux and Uy displacement maps. The artifacts are observed as stripes that strike in the NW-SE direction and seem to become more prominent as the displacement increases. Because the divergence maps are a construction of the displacement maps, the artifacts are also observed in these maps, but with a lower magnitude.

It is difficult to understand and pinpoint the exact origin of these artifacts. To the best of our knowledge, there are few reported cases of such artifacts occurring in our laboratory and elsewhere, especially with the high magnitude of occurrence. Hence, we reached out to one of the creators of MicMac for some guidance about these artifacts as we believe they originate from the MicMac processing. Unfortunately, the creator stated that there was no current solution to this problem, and a plausible cause of this might be due to aliasing. Aliasing can cause different signals to become indistinguishable when sampled. Consequently, as the signals are used to reconstruct the resulting signal, the latter can turn out differently compared to the original data.

We also believe that the texture might play a role in the intensity of the artifacts produced in our results. Orthophoto observations (fig. 3.5) show the pixel size versus the size of the texture, i.e., the olivine sand grains and the pixel size of the image, which seems to be about the same size. We believe that equal size distribution of pixel size versus texture size might cause aliasing. Aforementioned, this artifact error is still poorly understood and partakes in a broader issue related to these artifacts that require further investigation to determine the origin and intensity. The documentation of these artifacts is sparse, which implies that the high magnitude of artifacts produced in our experimental results can provide room for future investigation.

6.6 Future prospects

Experiments performed in the laboratory give rise to a number of questions that can be explored under certain conditions. With the limited time of a researcher, it is important to choose interesting approaches that (hopefully) can unravel fundamental aspects of volcanic processes. Conversely, being restricted to time and to a small number of parameters leave room for numerous unanswered questions related to dyke emplacement on surface deformation. A comprehensive study in the future should therefore include some aspects of the questions and comments described in the following section.

It is important to dig deeper into the mechanisms of dyke propagation, as this is still poorly understood. Dyke propagation is extremely complex and relies heavily on a wide range of factors (see a thorough description on dyke propagation in Galland et al. 2018). Over the last decades, the following questions have been highlighted. What is the three-dimensional shape of dykes that propagate? What control dyke dynamics and their geometry? What is the effect of an external stress field, free surface, layering and topography?

Contradiction still resides between the data obtained from established geodetic models and the experimental models. Henceforth, it directs attention to the challenge for the physical validity in simplistic models. The models need to include more complexity without sacrificing errors. However, current models still suffer significantly due to the complexity of the Earth.

Data obtained from the experimental models can still be improved through advances in the monitoring techniques and the experimental procedure. Optimizations on the photogrammetric methods to increase the resolution, both spatially and temporally, will further resolve the measured surface deformation. Although the current monitoring techniques have an extensive geoscientific potential, the data can might be a bit too overwhelming. The avalanche of all data needs to be embraced to exploit the outcome to the fullest. In addition, a more thorough investigation of the artifacts produced by the processing of Micmac is needed. A possible solution would, therefore, be to test the relative contribution of grain size versus pixel size on the artifact intensity.

In regard to the experimental constraints, there are still fundamental questions that ought to be addressed regarding the physical parameters in experimental modeling. Essentially, an integration of laboratory model results with multidisciplinary research is needed in terms of scaling of laboratory models. This requires rigorous dimensional analyses to provide

dimensionless experimental results so that it can overcome the problem that resides within the scaling of laboratory experiments. Furthermore, the boundary conditions in our experiments compared to geodetic models are different. Geodetic models usually have infinite boundary conditions, while our experiments have finite boundaries constricted to the experimental box.

Parameters within our experiments can be modified in a number of ways. This leads to questions that were not answered in our project: How will a different net with different rigidity control magma propagation? The meshed net can be oriented in endless possibilities. How would different intermediate net orientations influence magma propagation? How would the choice of a different magma analogue affect surface deformation? What effect does the forward pushing of plates on lateral dyke propagation and the associated surface deformation have? Moreover, what contribution would different crust model materials have on magma propagation and the resulting surface deformation?

The experiments in this Thesis were performed under lithostatic stress boundary conditions, which means that there were no contributions to regional tectonic stresses. Investigation of tectonic stretching on geodetic implications has been poorly described in the literature despite the clear occurrence of tectonic influence at volcanic rifts. Future studies should therefore include such extensional stress conditions to investigate the relative contributions of the extensional forces of tectonics and dyke emplacement on surface deformation. Performing such experiments could challenge the experimental modeler, as it is arguably difficult to determine whether the surface deformation is induced by the actual magma ascending to the crust or if it is a product of the actual tectonic stresses. Another difficult consideration is the aforementioned anisotropic and topographic effects on surface deformation. However, to simplify model assumptions is a requirement due to the Earth's heterogeneity for which the details are unknown (Heimisson, 2015). Regardless of the importance of the latter questions, with the current experimental model setup, we believe that focusing on model complexities that are far too complex might give results that are less physically relevant. Overcomplicating an arguably simplistic laboratory approach might distill from the simplistic fundamentals that lie within experimental modeling.

7 Conclusive remarks

This thesis aimed to investigate lateral dyke propagation and its contribution to surface deformation. The outcome is integrated to provide geodetic implications and to test the physical relevance of the main geodetic models. The project is built on quantitative laboratory experiments designed to contribute an understanding of lateral dyke propagation in cohesive Coulomb silica flour. The resulting surface deformation was monitored through a photogrammetric system that produced high temporal and spatial resolution. The conclusions of this study are summarized in the section below.

1. Our experiments highlight enhanced confidence in using a meshed net as an experimental parameter for lateral dyke propagation.
2. Laterally propagating dykes produced broader central displacement pattern, more rounded DEMs and extensional fractures that strikes in the EW direction compared to the reference experiment. This highlights subtle insights in geodetic signals of propagating dykes, which could potentially be valuable for volcanic eruption forecasting. However, there is still a lot more to unravel in the unexplored pathways of propagating dykes.
3. We infer a two-stage dyke propagation evolution. Stage one is defined by the dyke propagation aligned parallel to the net in a high confinement environment, which produces low magnitudes of uplift. The second stage delineates the upward propagation of the dyke, resulting in an uplift acceleration.
4. The misfit between geodetic models and our experimental models imply that the geodetic models are not sufficient for delineating a sound physical interpretation of geodetic data. Our models could of course, also be physically invalid. What is known is that including Mohr-Coulomb materials in our experiments does provide different results than the classic models. This might call for new developments in models accounting for more complex behavior of magma propagation.
5. Our experimental approach still suffers from a lot of limitations. The experimental validity is highly dependent on being properly scaled and rigorous dimensional analysis. Experimental errors are also heavily dependent on the experimental modeler. The accuracy of the results is delineated by the experimental procedure and the photogrammetric system.

6. The photogrammetric setup is a generally viable monitoring technique for our laboratory approach, which produces high spatial and temporal data. The techniques can still be optimized with methods giving higher accuracy and resolution, which is an important aspect of surface deformation interpretation.
7. Our experimental model is by far complete to give a thorough representation of laterally propagating dykes. A comprehensive study on lateral propagation and the imposed surface deformation is defined by a wide range of experimental parameters that take into account Earth's complex nature. Considerations of Earth's complexities should in the future be taken into account to enhance the physical validity of our laboratory experiments.

References

Abdelmalak, M., Mourgues, R., Galland, O., & Bureu, D. (2012). Fracture mode analysis and related surface deformation during dyke intrusions: Results from 2D experimental modeling. *Earth and Planetary letters*. Vol. 359-360. Pp 93-105. Doi: https://doi.org/10.1016/j.epsl.2012.10.008

Bemis, S., Micklethwaite, S., Turner, D., James, M., Akciz, S., Thiele, S., & Bangash, H. (2014). Ground-based and UAV-based photogrammetry: A multi-scale, high-resolution mapping tool for structural geology and paleoseismology. *Journal of Structural Geology*. Volume 69. Pages 163-178. doi: https://doi.org/10.1016/j.jsg.2014.10.007

Ben-Zion, Y. (2017). On different approaches to modeling. *J. Geophys. Res. Solid Earth*. 122, 558–559, doi:10.1002/2016JB013922.

Bertelsen, H., S., (2019*).* Beyond Elasticity: An Experimental Study of Magma Emplacement Mechanisms and Associated Deformation Structures. *Faculty of Mathematics and Natural Sciences*. University of Oslo.

Bertelsen, H., S., Guldstrand, F., Galland, O., Sigmundsson, F., Pedersen, R., Mair, K., (2019). Beyond elasticity: Are Coulomb properties of the Earth's crust important for volcano geodesy? *Physics of Geological processes*. The NJORD Center. University of Oslo.

Bisson, M., Spinetti, C., Neri, M., Bonforte, A. (2015). Mt. Etna volcano high-resolution topgraphy: airborne LiDAR modelling validated by GPS data. *International Journal of Digital Earth*. Volume 9. Issue 7. Doi: https://doi.org/10.1080/17538947.2015.1119208

Bürgmann, R., & Thatcher, W. (2013). Space geodesy: A revolution in crustal deformation measurements of tectonic processes. *Geological society of America special papers*. 500, 396-430

Birdseye, C., H. (1940). Stereoscopic Phototopographic mapping. *Ann. Assoc. Am. Geogr*., 30. pp. 1-24, 10.1080/00045604009357193

Cayol. V., & Cornet, F., H. (1998). Three-dimensional modeling of the 1983-1984 eruption at Piton de la Fournaise Volcano, Reunion Island. *Journal of Geophysical Research*. 103.

Dai, F., Feng, Y. and Hough, R. (2014). 'Photogrammetric error sources and impacts on modelling and surveying in construction engineering applications'. *Visualization in engineering* 2(2). 1–14.

Daniels, K. A., Menand, T. (2015). An experimental investigation of dyke injection under regional extensional stress. *Journal of Geophysical Research: Solid Earth*. Vol. 120. Doi: https://doi.org/10.1002/2014JB011627

Dong-Hyun, K. (2016). Study on the Accuracy of Rock Surface Roughness Data using Close Range Photogrammetry. *Griffith School of Engineering*. Ph.D Thesis

Dzurisin, D., (2007*).* Volcano Deformation Geodetic Monitoring Techniques. *Springer-Praxis books in geophysical sciences*. Chicester. 1st edition.

Eaton, J., P. (1959). A Portable Water-tube Tiltmeter. *Bulletin of the Seismological Society of America*. 49 (4): 301–316.

Fabris, M., Pesci, A. (2005). Automated DEM extraction in digital aerial photogrammetry: precisions and validation for mass movement monitoring. *Annals of geophysics*. Vol. 48.

Galland, O., (2012). Experimental modelling of ground deformation associated with shallow magma intrusions. *Earth and Planetary Science Letters.* Vol. 317-318. Pp. 145-156. Doi: https://doi.org/10.1016/j.epsl.2011.10.017.

Galland, O., Cobbold, P. R., Hallot, E., de Bremond d'Ars, J., Delavaud, G. (2006). Use of vegetable oil and silica powder for scale modelling of magmatic intrusion in a deforming brittle crust. *Earth and Planetary Science Letters.* 243(3) pp. 786-804.

Galland, O., H. S. Bertelsen, F. Guldstrand, L. Girod, R. F. Johannessen, F. Bjugger, S. Burchardt, and K. Mair. (2016*).* Application of open-source photogrammetric software MicMac for monitoring surface deformation in laboratory models. *J. Geophys. Res. Solid Earth*. 121.

Galland, O., Holohan, E., Van Wyk de Vries, B., Burchardt, S. (2018). Laboratory Modelling of Volcano Plumbing Systems: A Review. *Phyiscal Geology of Shallow Magmatic Systems*. pp 147-214.

Galland, O., Planke, S., Neumann, E. R., Malthe-Sørenssen, A. (2009). Experimental modelling of shallow magma emplacement: application to saucer-shaped intrusions. *Earth and Planetary Science Letters*. 277(3). pp 373-383.

Galland, O., Burchardt, S., Hallot, E., Morgues, R. & Bulois, C. (2014). Dynamics of dikes versus cone sheets in volcanic systems. *JGR Solid Earth.* Vol. 119, Issue 8. Pp. 6178-6192. Doi: https://doi.org/10.1002/2014JB011059.

Gudmundsson, A., (1983). Form and dimension of dykes in eastern Iceland. *Tectonophysics*. Vol. 95 Issue 3-4. Pp. 295-307. Doi: https://doi.org/10.1016/0040-1951(83)90074-4

Guldstrand, F. (2018*).* Quantitative Laboratory Modelling of Host Rock Deformation due to the Intrusion of Magma. *Faculty of Mathematics and Natural Sciences.* University of Oslo.

Guldstrand, F., Burchardt, S., Hallot, E., & Galland, O. (2017). Dynamics of surface deformation induced by dikes and cone sheets in a cohesive Coulomb brittle crust. *Journal of Geophysical Research: Solid Earth*, 122. https://doi.org/10.1002/ 2017JB014346.

Hall J (1815) II. On the Vertical Position and Convolutions of certain Strata, and their relation with Granite. *Earth Environ Sci Trans R Soc Edinburgh* 7(1):79–108. doi: 10.1017/S0080456800019268.

Handin J., Carter N. (1987). Rheology of rocks. In: *Structural Geology and Tectonics.* Encyclopedia of Earth Science. Springer. Berlin. Heidelberg. Doi: https://doi.org/10.1007/3-540-31080-0.

Heimisson, E., R. (2015). LATERAL DIKE PROPAGATION FORECASTING MODEL. *School of Engineering and Natural Sciences*. University of Iceland. Reykjavik.

Hubbert, M., K. (1937). Theory of scale models as applied to the study of geologic structures. *Geol. Soc. Am Bull* 48:1459–1520.

Kervyn M., Ernst GGJ., van Wyk de Vries B., Mathieu L., Jacobs P. (2009) Volcano load control on dyke propagation and vent distribution: insights from analogue modeling. *J. Geophys Res.* 114(B3):B03401. doi:10.1029/2008jb005653

Lim, K., Treiz, P., Wulder, M., St-Onge, B., & Flood, M. (2003). LiDAR remote sensing of forest structure. *Progress in Physical Geography: Earth and Environment*. Vol 27. doi: https://doi.org/10.1191/0309133303pp360ra

Lisowski, M. (2007). Analytical volcano deformation source models in Bondel. *Volcano deformation: new geodetic monitoring techniques.* Springer Praxis books, Chichester, pp. 279-304.

Mastin LG., Pollard DD. (1988). Surface deformation and shallow dike intrusion processes at Inyo craters, Long Valley, California. *J. Geophys .Res* 93(B11):13221– 13235

McGuire WJ., Pullen AD. (1989). Location and orientation of eruptive fissures and feeder dykes at Mount Etna; influence of gravitational and regional tectonic stress regimes. *J. Volcanol. Geotherm. Res.* 38(3–4):325–344

Mogi, K., (1958). Relations between the eruptions of various volcanoes and the deformation of the ground surfaces around them. *Bull Earthq*. Inst U Tokyo, 36, 99-134

Okada,Y. (1985). Surface Deformation due to shear and tensile faults in a half space. *Bulletin of the Seismological Society of America*. Vol. 75. No. 4 pp. 1135-1154.

Pinel V., Jaupart C. (2000). The effect of Edifice load on magma ascent beneath a volcano. *Philos. Trans: Math Phys Eng Sci* 358(1770):1515–1532

Pollard DD., Holzhausen G. (1979). On the mechanical interaction between a fluid-filled fracture and the Earth's surface. *Tectonophysics* 53(1–2):27–57

Pollard DD., Johnson AM. (1973). Mechanics of growth of some laccolithic intrusions in the Henry Mountains, Utah, II. Bending and failure of overburden layers and sill formation. *Tectonophysics* 18:311–354

Ralph O., Dubayah., Drake, J., B. (2000). Lidar Remote Sensing for Forestry. *Journal of Forestry*. Volume 98. Issue 6. June 2000, Pages 44–46. https://doi.org/10.1093/jof/98.6.44

Rivalta, E., Taisne, B., Bunger, A., P., Katz, R., F. (2014). A review of mechanical models of dike propagation: schools of throught, results and future directions. *Tectonophysics* 638 (2015) 1-42.

Robock, A. (2000). Volcanic eruptions and climate. *Reviews of Geophysics*. Volume 38. Doi: https://doi.org/10.1029/1998RG000054.

Rubin, M., A. (1992). Dike-Induced Faulting and Graben Subsidence in Volcanic Rift Zones. *Jour. Geophys.* Vol. 97. P 1839-1858.

Rubin, M., A. (1993). Dike-Induced Faulting and Graben Subsidence in Volcanic Rift Zones. *Journal of geophysical research*. vol. 96, pp. 1839-1858.

Rubin, M., A. (1995). PROPAGATION OF MAGMA-FILLED CRACKS. *Earth planetary science.* 23:287-336

Ruegg, J. C., Lepine, J., C., Tarantola, A., & Kasser, M. (1979). GEODETIC MEASUREMENTS OF RIFTING ASSOCIATED WITH A SEISMO-VOLCANIC CRISIS IN AFAR. *Geophys. Research letters*. Vol. 6. NO 11.

Rupnik, E., Daakir, M. and Pierrot Deseilligny, M. (2017). 'Micmac – a free, open-source solution for photogrammetry', *Open Geospatial Data, Software and Standards* 2(1), 1–9.

Sigmundsson, F. (2016). New insights into magma plumbing along rift systems from detailed observations of eruptive behavior at Axial volcano. *Geophys. Res. Lett*. 43, 12,423–12,427, doi:10.1002/2016GL071884.

Sigmundsson, F. (2018). Magma Movements in Volcanic Plumbing Systems and their Associated Ground Deformation and Seismic Patterns. *Volcanic and Igneous Plumbing systems.* Doi:http://dx.doi.org/10.1016/B978-0-12-809749-6.00011-X

Sigurdsson, H., & Sparks, R., (1978). Petrology of Rhyolitic and mixed magma Ejecta from the 1875 Eruption of Aska, Iceland. *Journal of Petrology*. Vol 22. Pp. 41-84. Doi: https://doi.org/10.1093/petrology/22.1.41

Spacapan, J., & Galland, O., & Leanza, H., & Planke, S. (2016). Igneous sill and finger emplacement mechanism in shale-dominated formations: a field study at Cuesta del Chihuido, Neuquén Basin, Argentina. *Journal of the Geological Society*. 174.

Thompson, R., A., & Schilling, S., P. (2007). Volcano deformation: new geodetic monitoring techniques. *Springer Praxis books*. Chichester. pp. 195-222.

Tibaldi, A. (2015*).* Structure of volcano plumbing systems: a review of multi-parametric effects. *Journal of Volcanology and Geothermal Research.* Vol. 298, pp. 85-135. Doi: https://doi.org/10.1016/j.jvolgeores.2015.03.023.

Tong, X., Sandwell, D., T., and Smith B. (2013). High-resolution interseismic velocity data along the San Andreas Fault from GPS and InSAR. *JGR Solid Earth.* vol. 118. pp. 369-389. Doi: https://doi.org/10.1029/2012JB009442

Trippanera, D., J. Ruch, V. Acocella, and Rivalta, E. (2015). Experiments of dike-induced deformation: Insights on the long-term evolution of divergent plate boundaries. *J. Geophys. Res*. Solid Earth, 120, 6913–6942.

Trippanera, D., V. Acocella, and Ruch, J. (2014). Dike-induced contraction along oceanic and continental divergent plate boundaries. *Geophys. Res. Lett*., 40.

Wright, T. J., Ayele, A., Ferguson, D. J., Kidane, T. & Vye-Brown, C. (2016). Magmatic Rifting and Active Volcanism. *Geological Society. London. Special Publications*. 420, 1–9. First published online July 6, 2016, http://doi.org/10.1144/SP420.18.

Appendix A

Experimental setup procedure

The box

1. Clean your environment and box before starting. A clean working space is crucial when working in a lab.

2. Plug the inlet in the box.

3. Cut your net into the height you want to use.

4. Tape the net on the vertical walls of the box. Make sure you stretch the net, making it as rigid as possible.

5. Attach the two loose vertical walls to create a higher box that can contain more sand. Make sure the screws in the walls are accessible to you.

6. Tighten the box with metal screws and make sure there are no gaps in between the fiberglass and the floor of the box.

7. Put your box in “the cage”. The doors should be facing towards you.

8. Put on a lab coat and mask.

The sand

9. Measure silica flour in a smaller box on a weight and carefully load the experimental box with the sand.

10. Measure around 3 kg segments of sand and pour it in the large experimental box.

11. Evenly distribute the sand and level it often when pouring the sand.

12. Be careful when pouring the sand onto the net. Make sure it stays vertical and is as rigid as possible throughout the process.

13. When you have the amount of desired sand, level it, and clean the small box and the weight.

14. For compaction, connect the Houston Vibrator to the bottom of the box and make sure the arrows on the shaker always point counterclockwise as this determines the shaking direction.

15. Carefully place the metal plate used for compaction on top of the sand. This will make sure the sand is evenly leveled and stays as horizontal as possible.

16. Attach four clamps at each corner of the box with equal compression to secure the box from collapsing when compacting the sand.

17. Add wet paper at the bottom of the box, which will soak up the excess sand that falls out of the box under compaction.

18. Open the window and turn on the air fan and check the airflow direction.

19. Put the side blowing out the air on the outside of the window and the other end of the fan just above the box.

20. Open the excel sheet for compaction called “Compaction”. This program calculates the density after each shaking.

21. This is done by measuring the depth of each corner after compaction. As we already know how much silica flour is put in the box, we can calculate the density by measuring the height of the leveled sand.

22. Turn on the air pressure and put it to 3 bars.

23. Start the shaker for 30 seconds intervals and measure the height of each corner after each shaking.

24. Make sure each of the corners is as evenly leveled as possible to produce a flat initial surface.

25. Start a new shaking until the density is 1050kg/cm^3

26. Turn off the air pressure and disconnect the vibrator from the box.

27. Carefully remove the metal plate.

28. Remove all clamps that are attached to the box.

29. Remove the excess sand that fell out of the box during the compaction.

30. Remove the loose vertical walls.

31. Place GCP markers on each of the corners of the box.

32. On your flat initial surface, add coffee grains and olivine sand to produce a texture on the surface.

The photogrammetric setup

33. Insert SD-cards and batteries to the four cameras.

34. Make sure all cameras have settings put on ISO:200, aperture value (F) 11, 1/60.

35. Put the cameras in their position on top of the cage. Each camera is numbered from 1 to 4 with respective positions, also numbered 1 to 4.

36. Camera number 1 is directly above the box. The others are at a slight angle around camera 1. Each camera must be put into position 1 and focused correctly.

37. Remove camera number 1 and place camera number 2 on position 1.

38. Put the camera on autofocus and focus on the flat initial surface of the box. Slightly press the picture capture button on the camera until the square on the camera screen turns green, and the camera is focused.

39. Turn the camera to manual focus and put camera number 2 back to its respective position.

40. Repeat this process until all cameras are focused on the box

41. Finally, put camera 1 back into its position and focus it on the same procedure done in the previous steps.

The volumetric pumping system

42. Remove the inlet plug and attach the inlet tube to the pipe of the box.

43. Connect all tubes, as shown in the pictures.

44. Make sure they are tied enough by pulling them. This is a crucial step as having to lose connected tubes often makes the pressure from the oil disconnect the tubes creating an oil spill.

45. Heat water in a container up to about 60 degrees

46. While it heats, turn on the computer and connect the “T-switch” to power.

47. Connect the USB cable

48. Turn on the volumetric pump and circulate the water throughout the system.

49. Open the program “Labinux” and test the atmospheric pressure by running the program.

50. Check the tubes for air bubbles and try to eliminate the bubbles in the system.

51. Now connect the “T-switch” to the Arduino box called “trigger box”.

52. Connect the cameras to the Arduino box called “camera box” and connect this box with the “trigger box”.

53. Close all windows and close the curtains.

54. Put on extra light for optimal images.

55. Do some test runs before running the experiments. Check that everything is connected to the trigger box and flick this switch to on.

56. Check that the pressure gauge works, the cameras take synchronized images and that the volumetric system works.

57. Heat up vegetaline oil to about 60 degrees.

58. Now run oil through the volumetric system and check that everything works again.

59. Make sure to remove air bubbles in the oil.

60. Now finally attach the tube system to the inlet tube.

61. Erase all data from the cameras and the pressure gauge.

62. We are now about to run the experiment!

63. Set the “trigger box” on and start the timer.

64. Stop the experiment when oil has breached the surface and write down the run time for the experiment.

65. Disconnect the inlet tube and run warm water through the system for around 20 minutes.

66. Turn off the cameras and store the images on your computer.

67. Wait 40 minutes for the oil inside the silica flour to solidify.

Excavating the intrusion

68. After the oil is solidified, carefully unscrew one side of the wall. As the silica flour is cohesive, the vertical walls will prevent it from falling.

69. Open the window and start the air fan.

70. Take a spatula and remove the top layer of the surface that contains coffee and olivine sand grains. Throw this in the garbage bin.

71. Carefully remove the silica flour bit by bit and put it in the silica flour container until you reach the solidified intrusion.

72. Use a specimen brush and gently brush the intrusion until the silica flour is brushed off.

73. Remove the cage and the fan.

74. Remove the rest of the fiberglass walls of the box.

75. Clean of the table and the box for excess silica flour.

76. Place cardboards around the intrusion. This gives texture around the intrusion to help the photogrammetric analysis.

77. Take several images of the intrusion. One set of images from the four cameras on top of the cage. One set of images that are close up (30 cm) and one set of images that are at an

intermediate distance (2 m). Make sure to take at least four pictures from different angles at each set of images.

78. Repeat step 77 for all the sides of the intrusion.

79. Store all the images from the SD cards on your computer.

Appendix B

Scripts MicMac

All the scripts derived from our experimental data processing in MicMac are listed in the GitHub link below. All scripts are provided by the Physics of Geological Processes group at the University of Oslo.

https://github.com/FrankGuldstrand/micmac_workflows

Appendix C

Matlab scripts

All scripts were generated by the Physics of Geological Processes at the University of Oslo. Modifications of these scripts are made by me, as provided in the Github link below.

https://gist.github.com/danielabrahamsen1

Appendix D
Figures

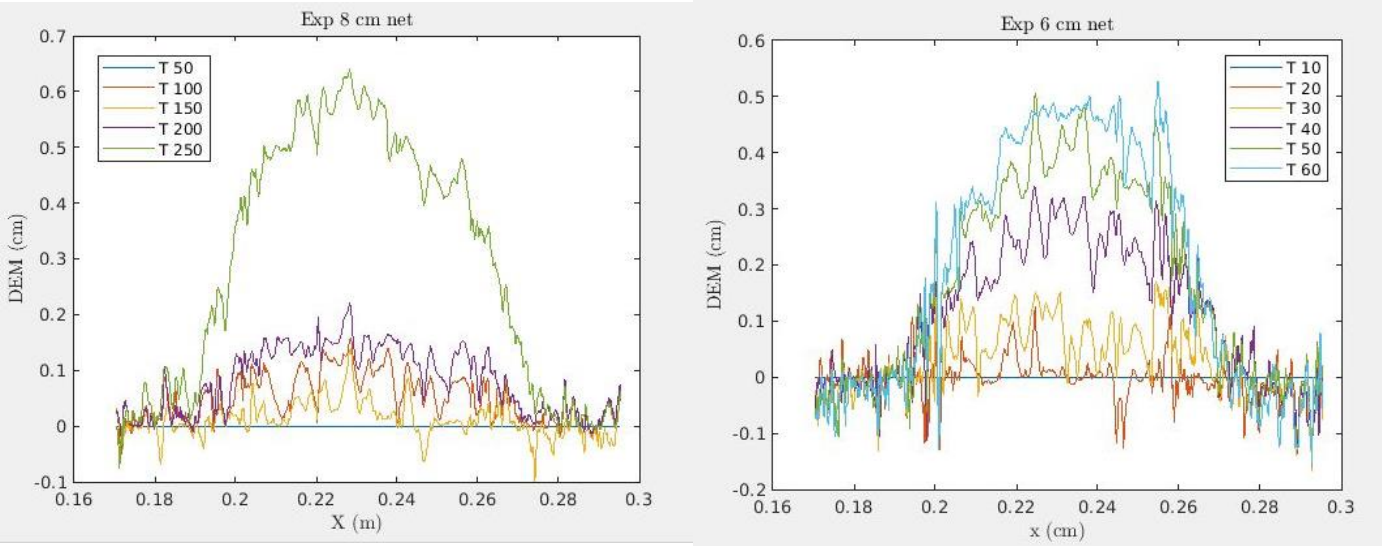

Figure 1: DEM versus a transect aligned parallel to the net for experiment 8 cm (right) and experiment 6 cm (right)

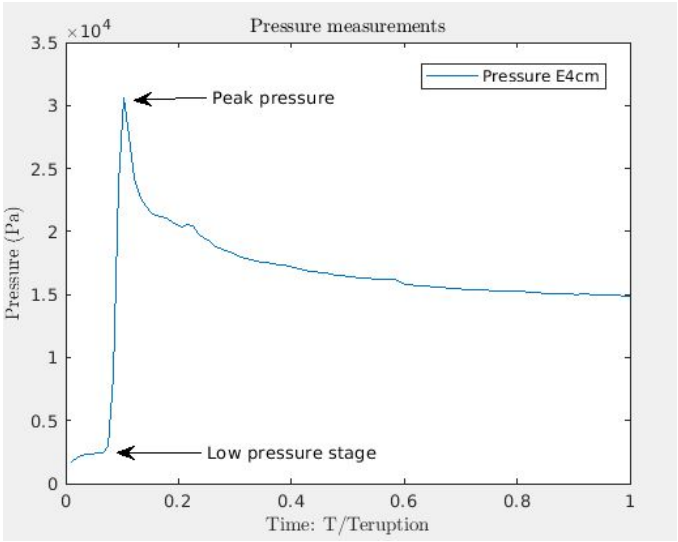

Figure 2: The figure shows pressure measurements from experiment 4 in the silica flour experiment as a function of time T scaled by the experiment duration $T_{eruption}$. Note that the pressure gauge was unfortunately destroyed and provided incomplete pressure data. The only experiment that gave reasonable pressure data were from experiment 4 cm seen in the figure above.